JGR Space Physics

RESEARCH ARTICLE
10.1029/2024JA033431

Jupiter's Auroral Ionosphere: Juno Microwave Radiometer Observations of Energetic Electron Precipitation Events

Ananyo Bhattacharya[1], J. Hunter Waite[2], Steven M. Levin[3], Fabiano A. Oyafuso[3], Paul G. Steffes[4], Yue Lu[4], G. Randall Gladstone[5], Joshua Kammer[5], Tom A. Nordheim[6], Chris Paranicas[6], Thomas Cravens[7], James Sinclair[3], Jiheng Hu[1], Cheng Li[1], Sushil K. Atreya[1], Heidi N. Becker[3], and Scott J. Bolton[5]

[1]Department of Climate and Space Sciences and Engineering, University of Michigan, Ann Arbor, MI, USA, [2]Department of Physics and Astronomy, The University of Alabama, Tuscaloosa, AL, USA, [3]NASA Jet Propulsion Laboratory, California Institute of Technology, Pasadena, CA, USA, [4]School of Electrical and Computer Engineering, Georgia Institute of Technology, Atlanta, GA, USA, [5]Southwest Research Institute, San Antonio, TX, USA, [6]Johns Hopkins University Applied Physics Laboratory, Laurel, MD, USA, [7]Department of Physics and Astronomy, The University of Kansas, Lawrence, KS, USA

Key Points:

- Electron precipitation in Jupiter's northern aurora can increase microwave opacity, appearing as cold spots in MWR antenna temperature
- Precipitation of 32 keV–10 MeV electrons results in ionization of the lower stratosphere producing short-lived hydrocarbon ions
- Rapid changes in MWR antenna temperatures over Juno spin period highlight short-time scale temporal variations in the ionospheric medium

Correspondence to:
A. Bhattacharya,
ananyo@umich.edu

Citation:
Bhattacharya, A., Waite, J. H., Levin, S. M., Oyafuso, F. A., Steffes, P. G., Lu, Y., et al. (2025). Jupiter's Auroral ionosphere: Juno Microwave Radiometer observations of energetic electron precipitation events. *Journal of Geophysical Research: Space Physics*, *130*, e2024JA033431. https://doi.org/10.1029/2024JA033431

Received 13 OCT 2024
Accepted 29 JAN 2025

Author Contributions:
Conceptualization: Ananyo Bhattacharya, J. Hunter Waite, Steven M. Levin, Paul G. Steffes
Data curation: Fabiano A. Oyafuso, James Sinclair, Jiheng Hu
Formal analysis: Ananyo Bhattacharya, J. Hunter Waite, Fabiano A. Oyafuso, Yue Lu
Investigation: Ananyo Bhattacharya, Fabiano A. Oyafuso
Methodology: Ananyo Bhattacharya, J. Hunter Waite, Steven M. Levin, Paul G. Steffes, Yue Lu, G. Randall Gladstone, Joshua Kammer, Tom A. Nordheim, Chris Paranicas, James Sinclair, Cheng Li, Sushil K. Atreya, Heidi N. Becker
Resources: Steven M. Levin, Cheng Li, Sushil K. Atreya, Scott J. Bolton
Software: Ananyo Bhattacharya, J. Hunter Waite, Fabiano A. Oyafuso,

© 2025 The Author(s).
This is an open access article under the terms of the Creative Commons Attribution-NonCommercial License, which permits use, distribution and reproduction in any medium, provided the original work is properly cited and is not used for commercial purposes.

Abstract Jupiter's polar aurora exhibits low brightness temperatures in Juno Microwave Radiometer (MWR) observations when the Juno spacecraft passes over the high-latitude region of the Northern Hemisphere. These cold features are observed predominantly at 0.6 GHz and show both long-term ~ hours and short-term changes over time, that is, spans less than the 30-s spacecraft spin period. The MWR "cold spot" observations are associated with polar ultraviolet emission features that are thought to originate from high energy electron precipitation into the Jovian high latitude atmosphere. The energetic electron precipitation produces strong absorptive characteristics at microwave frequencies due to the transient formation of high-density electron regions in the lower stratosphere. In this paper, we describe progress on the analysis of Juno MWR observations of the northern aurora and simulate the effects of heating and electron impact ionization processes due to high energy particle precipitation events in Jupiter's auroral ionosphere. Electron precipitation intensities at energies up to 10 MeV inferred from the Jupiter Energetic-Particle Detector Instrument (JEDI) and Ultraviolet Spectrograph (UVS) instruments are used as a Northern Hemisphere case study to understand the energy deposition and ionization processes in the lower stratosphere, and subsequently used to estimate the microwave and ultraviolet opacity of the auroral region. The northward progression of Juno's perijove during the mission reduces the overflight altitude and allows important insights into effects produced at different length scales with respect to the auroral oval.

Plain Language Summary Electrons with energies higher than 500 MeV lead to production of enhanced electron density regions in Jupiter's high-latitude lower stratosphere, depositing a large amount of energy responsible for contributing to heating and ionization processes. These regions have electron densities much higher than the non-auroral ionosphere of Jupiter and the ionosphere of Earth at corresponding atmospheric pressure levels, and result in strong absorption at microwave frequencies of about 1 GHz. It is attributed to collision of free electrons with atmospheric neutral constituents. The generally elevated electron densities within the main aurora exhibit a significant reduction in antenna temperatures measured by Juno Microwave Radiometer passes over Jupiter's Northern Aurora. We use the intensity of downward directed electrons measured by the JEDI and UVS instruments, and determine their contribution to local ionization processes. Dramatic transient events that vary within a 30 s time span are also observed, attributed to rapid variations in local electron flux and fast dissociative recombination of hydrocarbon ions produced in the lower stratosphere. Variations in intensity and energy of electron flux, changes in the MWR antenna footprint relative to the auroral oval and spatial extent of electron beams collectively contribute to the variations in MWR "cold spot" temperatures.

1. Introduction

Planetary aurorae result from energetic electron or ion impingement into the gaseous envelope of a planet. The particles are accelerated by plasma and wave processes that in the case of magnetized planets result from interactions with the solar wind or from internal magnetospheric dynamics. In many cases, these processes lead to the redistribution of momentum and energy within the system through field-aligned currents, which consequently

Yue Lu, Tom A. Nordheim, Thomas Cravens, James Sinclair, Jiheng Hu, Cheng Li
Supervision: J. Hunter Waite, Steven M. Levin, Cheng Li, Sushil K. Atreya
Validation: Ananyo Bhattacharya, J. Hunter Waite, Tom A. Nordheim
Visualization: Ananyo Bhattacharya, Yue Lu, Jiheng Hu
Writing – original draft: Ananyo Bhattacharya, J. Hunter Waite, Steven M. Levin, Paul G. Steffes, Yue Lu, Tom A. Nordheim, James Sinclair, Cheng Li, Sushil K. Atreya
Writing – review & editing: Ananyo Bhattacharya, J. Hunter Waite, Steven M. Levin, Paul G. Steffes, Yue Lu, G. Randall Gladstone, Joshua Kammer, Tom A. Nordheim, Chris Paranicas, Thomas Cravens, James Sinclair, Cheng Li, Sushil K. Atreya, Heidi N. Becker, Scott J. Bolton

accelerate charged particles to very high energies by wave-particle interactions (B. H. Mauk et al., 2020; B. Mauk et al., 2023). As the energetic particles interact with the gaseous envelope of the planet, they dissipate their energy through ionization; production of x-rays, ultraviolet, and visible (non-thermal) emissions; molecular dissociation and resulting chemistry; and through heating of the atmospheric envelope, which results in atmospheric/ionospheric transport and increased infrared emission. The measurements from the Juno mission (Hodges et al., 2020; F. A. Oyafuso et al., 2023) have demonstrated that the aurora via its generation of a local plasma enhancement (ionosphere) also absorbs and reflects microwave wavelength emissions that are associated with the apparent cold spots in the microwave emission. These phenomena are exhibited by a local decrease in brightness temperatures at low frequencies (0.6–1.2 GHz) within the observation window of the Juno Microwave Radiometer. As a result of the latter, the process affects the high-altitude distribution of the planet's microwave radiation by absorbing and redistributing atmospheric microwave thermal emission at high latitudes, effectively acting as an opaque medium. The existence of this absorption is most apparent in the correlation when a map of the microwave radiation is overlayed onto the auroral oval observed by the Juno UltraViolet Spectrograph (UVS) (Hodges et al., 2020), which serves as an excellent proxy of the boundaries of Jupiter's auroral and polar cap precipitation regions.

Initial attempts to understand the cold spot brightness temperature of the radiated microwaves by Juno's onboard Microwave Radiometer (Janssen et al., 2017) were reported in (Hodges et al., 2020). They attribute the cold spots in brightness temperature to plasma reflection caused by the high density of electrons in the ionospheric medium. The electron density retrieved from plasma reflection theory amounts to $\sim 10^9$ cm^{-3} that is, 100 times higher than past estimations of Jupiter's steady-state auroral processes (Waite Jr et al., 1983). It was also inconsistent with the few auroral radio occultation experiments conducted by Galileo at 68° and 76° N latitudes. Past radio occultations provided limited coverage of auroral ionospheric structure and its variability (Mendillo et al., 2022). However, as the Juno spacecraft increased its coverage of in situ measurements within the Jovian magnetosphere, several transient events with highly energetic electrons and ions and large energy fluxes (≥ 1 W m^{-2}) began to emerge (B. H. Mauk et al., 2017; B. Mauk et al., 2018; Bonfond et al., 2018). Here, we demonstrate through modeling that this high-energy flux carried by MeV electrons can generate a large amplitude transient ionospheric layer much deeper in the atmosphere than previously expected and at altitudes where the electron collision frequency with the neutral atmosphere produces a unique microwave absorption regime.

Microwave absorption processes at centimeter wavelengths have been shown in the case of the Earth to occur in atmospheric/ionospheric regimes with both low and high values of neutral density (Woo & DeGroot, 1984). In the case of the low neutral density regimes, ionospheric plasma exhibits absorption of high-frequency radio waves (Harada et al., 2023; Rogers et al., 2015). In Jupiter's ionospheric medium due to the existence of considerable electron fluxes with energies exceeding 500 keV, large amounts of energy are deposited at lower altitudes (higher neutral pressures) as a result of the decreased stopping power for high energy electrons in H_2. These energetic electron precipitation events produce significant transient ionization that affect the propagation of the microwave radiation in the high-density regime. This stands in contrast with the previous explanation for the decrease in microwave brightness temperatures in the Jovian auroral zone (Hodges et al., 2020) put forward earlier, which stated the auroral ionosphere to be a strongly reflecting medium.

In order to study both the transient nature of the phenomena and to account for the unexpectedly high energy of the incoming electrons, we constructed a new auroral energy deposition model that combines a continuous slowing-down approximation (CSDA) of energetic particles (Padovani et al., 2009) with discrete energy loss modeling at electron energies below 10 keV (Waite Jr et al., 1983) to determine the ionization and thermal heating of the atmosphere. The ion production, chemical reactions, and thermal dissipation resulting from the auroral energy deposition were integrated into a time-dependent model of Jovian atmospheric chemical kinetics, tracking the charged particle production and loss processes. The model is then used to calculate the microwave absorption and reflection processes to assess the impact of locally generated ionospheric layers on the transmission of microwaves in the high-latitude atmosphere. These simulations are summarized in a schematic diagram in Figure 1.

2. Methodology

2.1. Juno MWR Data Processing

The Juno Microwave Radiometer (MWR) is a 6-channel (0.6–22 GHz) passive microwave instrument designed to penetrate the clouds and measure the temperature and composition of Jupiter's neutral atmosphere at pressures as

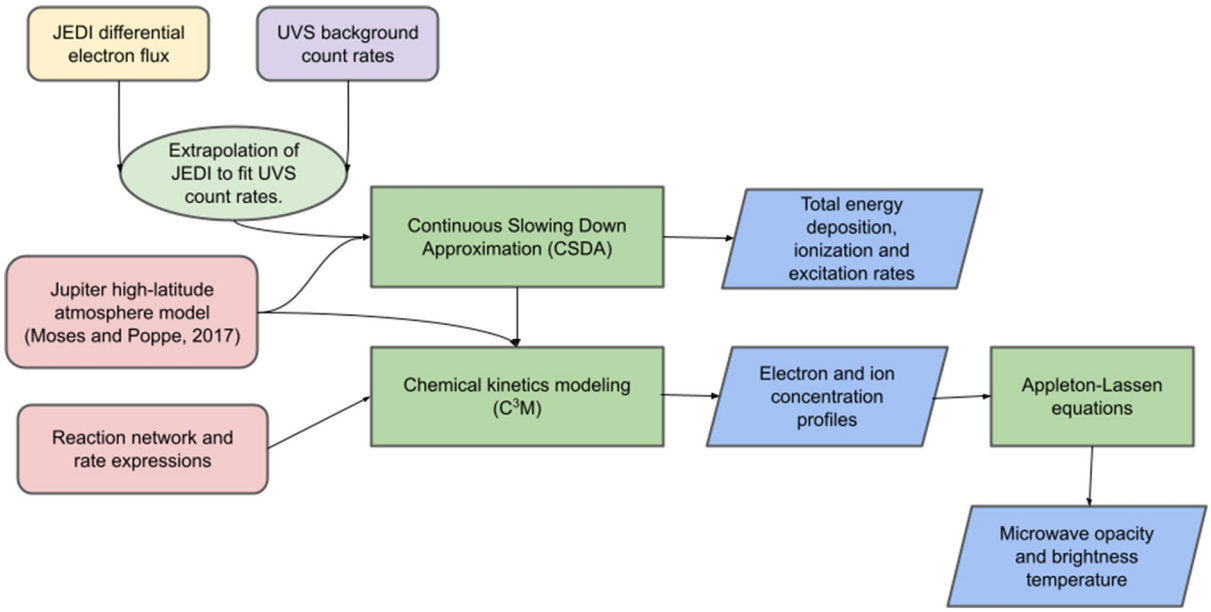


Figure 1. Schematic of atmospheric models, inputs and outputs applied to simulate electron precipitation and microwave opacity of Jupiter's auroral ionosphere.

high as a few hundred bars (Janssen et al., 2017). Juno Microwave Radiometer collects data at a cadence of approximately one sample every 100 ms, while the Juno spacecraft rotation sweeps the antenna beam over the planet approximately twice per minute. Jupiter's atmospheric temperature increases with depth, so the lower frequencies, which emanate from deeper levels, observe higher temperatures. Typical brightness temperature observed by the 600 MHz channel is ∼900 K (F. Oyafuso et al., 2020), with latitudinal variation related to atmospheric composition and temperature (Li et al., 2017). The antenna temperature (T_A) measured by MWR is the integral of opacity times temperature, so any local variation in the opacity of the shallow atmosphere reduces the effective penetration depth, resulting in a lower observed T_A.

Juno perijove (PJ) observations provide a direct measurement of T_A at microwave frequencies. The T_A values at high latitudes exhibit cold features at 0.6, 1.2, and 2.2 GHz channels over the discrete auroral arcs (Hodges et al., 2020) and within the polar cap. The contrast between the cold spot brightness temperature and the background atmospheric temperature decreases at higher frequencies but is more prominent at 0.6 and 1.2 GHz. For our study, we consider T_A corresponding to PJ 1, 3–54 at 0.6 and 1.2 GHz from 50°N to the pole. The cutoff latitude for data filtering is chosen to be 50°N as cold spots have been observed between 50 and 90°N (Hodges et al., 2020).

2.2. Electron Precipitation and Energy Deposition

Throughout the Juno mission, electrons of energy higher than 1 MeV have been detected by the JEDI instrument near Jupiter's polar auroras (B. Mauk et al., 2018; Clark et al., 2018). We consider an extreme case of a charged particle precipitation event detected by JEDI during PJ 7 (B. Mauk et al., 2018). We further note from Figure 2 that there is a cold spot phenomenon observed during PJ 7. During this orbit, the MWR instrument observed a significant decrease in T_A, and a strong downward flux of precipitating electrons was measured near the same time on 11 July 2017 at 01:14:38 UTC. JEDI-integrated electron energy intensities are converted into differential intensity for the electron energy bins ranging from 32 keV to 1 MeV. For electrons ≥1 MeV, UVS omnidirectional background count rates are converted to extend the electron energy distribution to 10 MeV as per the method described in (Zhu et al., 2021). Electrons at energies greater than 1 MeV are expected to penetrate the stratosphere to much greater pressure levels, and cause a high degree of ionization below the methane homopause. We therefore seek to understand the ionization process in the lower stratosphere under various conditions of electron precipitation through modeling.

Atmospheric energy deposition and ionization due to collisional interactions with neutral species are simulated for a pure H_2 atmosphere. We apply continuous slowing-down approximation (CSDA) to compute electron

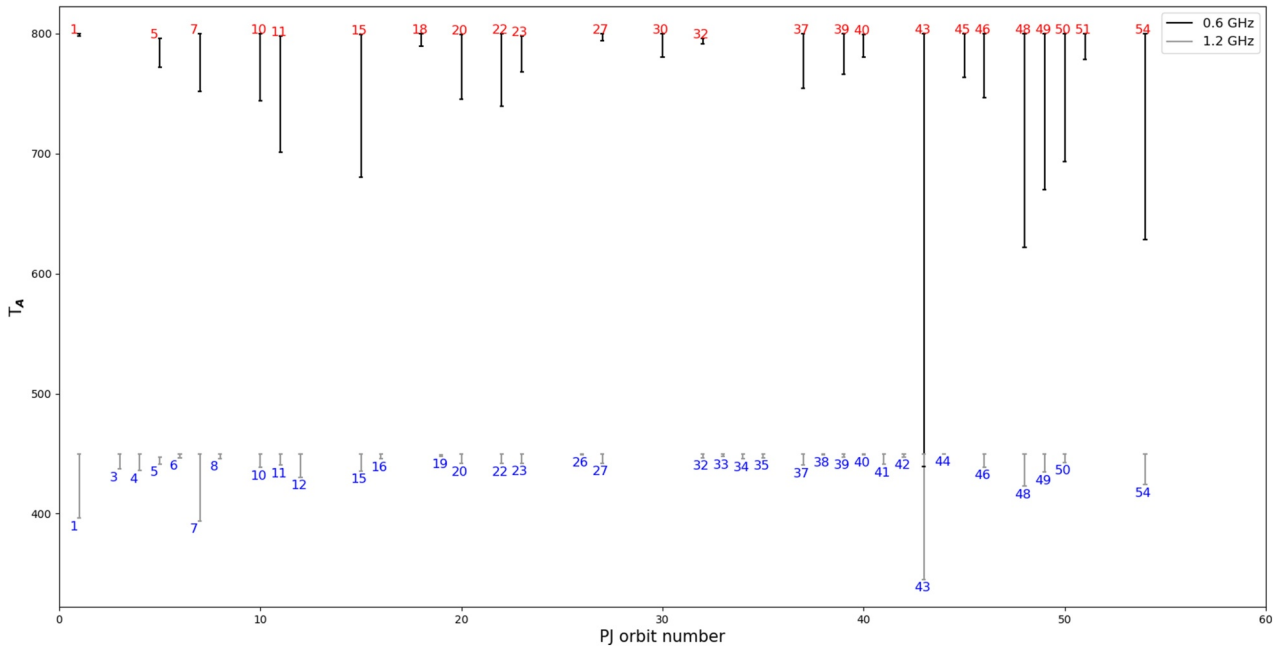


Figure 2. T_A corresponding to low-frequency channels filtered for emission angle less than 10°, and T_A magnitude less than the respective cutoff for PJ 1–54. Near-nadir values of T_A exhibit a large range with lower limits in ranges ∼450–750 K (0.6 GHz: black lines and PJ orbit in red), and 350–415 K (1.2 GHz: gray lines and PJ orbit in blue). Large dips in the T_A can be observed at both channels during multiple PJ orbits. A small range of T_A variability can also be attributed to atmospheric variations in both channels. Orbits with a large range in T_A magnitudes appear to be positively attributed to energetic precipitation events.

energy loss at an average 45° pitch angle using the loss function of H_2-e^- interactions provided in (Padovani et al., 2009). Effects due to the other constituents like He or CH_4 will be secondary to H_2. A high-latitude model of Jupiter's stratosphere from (Moses & Poppe, 2017) is adopted for the simulations. The total energy deposition is partitioned according to two-stream modeling in (Waite Jr et al., 1983) assuming primary electrons ∼10 keV. The energy partitioning is used to calculate rates for electron impact ionization, and direct excitation ($\nu_1 - \nu_3$) assuming ion-pair production of 39.38 eV per ion pair produced.

2.3. Time-Dependent Chemical Kinetics

The production and loss processes associated with the auroral ionosphere are expected to be rapidly changing due to changes in particle flux, and advection of neutrals and ions. To simulate the ion and electron concentration profiles, we solved time-dependent, one-dimensional reaction-diffusion equations for a system of neutrals, ions, and electrons. We have developed C^3M, a C++-based one-dimensional atmospheric chemistry model, to simulate ionospheric chemistry. It leverages the thermochemical reaction classes from Cantera (Goodwin et al., 2024) library to handle reaction data and calculate production rate, and the numerical Jacobian for a wide range of reactions including bimolecular and three-body reactions. We leverage the Cantera library to extend our application for electron impact ionization and H_2 vibrational chemistry. It also uses data structures from Athena++ library to handle the input and output files, which provides a robust code for multiple applications.

We adopted the high-latitude Jupiter atmosphere model from (Moses & Poppe, 2017) as the initial condition for temperature and hydrocarbon concentrations. Electron concentration profiles from a photochemically generated ionosphere represent a diurnally averaged initial condition of electrons, H^+, and H_3^+ concentration profiles. For a quasi-neutral approximation, we consider H^+, and H_3^+ concentrations to be 90% and 10% of the total electron concentration, maintaining a net neutral charge concentration. The model evolves the system of reactions relevant to the electron-impact process, and ion-neutral reactions. Electron precipitation contributes to vibrational excitation of H_2 molecules treated by a system of chemical reactions adopted from (Egert et al., 2017). Rate expressions of the chemical reactions along with their references are provided in Tables A1–A5 (check Appendix A for more information). For more detailed information, please refer to (Cravens, 1987; Egert et al., 2017). The model solves reactions for the following species: H_2, H_2^+, H^+, H, e^-, H_3^+, CH_4, CH_3^+, CH_4^+, CH_5^+, He, CH_3, $^1CH_2$,

$^3CH_2$, He^+, CH_2^+, CH^+, HeH^+, CH, C_2H_6, C_2H_5, C_2H_4, C_2H_3, C_2H_2, C_4H_6, C, C_4H_5, C_3H_6, C_2, C_2H, $H_2(\nu_1 - \nu_8)$, and $C_2H_5^+$.

Electron impact ionization of the hydrogen molecule is expressed in terms of rate per hydrogen molecule. Direct ionization rates are calculated from the total energy deposition rate by multiplying with the proportion of energy partitioned into H_2 ionization derived from two-stream transport models of Jupiter. Direct vibrational excitation of the first three states is derived using the same method. Vibrationally excited states for the hydrogen molecule $(\nu_1 - \nu_8)$, and vibrational cooling by hydrogen atoms have also been taken into account, considering collision processes described in (Cravens, 1987; Egert et al., 2017). These rate expressions have been adopted from a large set of theoretical calculations and laboratory results. We solve the following system of reaction-diffusion equations:

$$\frac{\partial q_i}{\partial t} = -\frac{\partial \phi_i}{\partial z} + R_i \tag{1}$$

$$\phi_i = -(K + D)Q\frac{\partial x_i}{\partial z} + Dq_i\left(\frac{1}{H_0} - \frac{1}{H_i} - \frac{1}{P_e}\frac{\partial P_e}{\partial z} - \frac{\alpha_i}{T}\frac{\partial T}{\partial z}\right) \tag{2}$$

Here, q_i is the number density of species i, ϕ_i is the vertical flux of species i through a given point in the atmosphere, Q is the total number density, R_i is the net production rate that is, sum of all chemical source, and sinks. K is the eddy diffusion coefficient, D_i is molecular/ambipolar diffusion coefficient, and x refers to the mole fraction of a given chemical species i. H_0 is the average well-mixed atmospheric scale height, and H_i is the scale height corresponding to a given atomic or molecular species. For ions, ambipolar diffusion has been taken into account with an additional term due to the electron pressure gradient. P_e is electron pressure, and it is relevant to ambipolar diffusion in ions (Nakamura et al., 2022). α_i refers to thermal diffusion coefficient. Thermal diffusion is important for H, and He, and it is set to zero for all other species (Krasnopolsky, 2019).

C^3M uses a semi-implicit scheme to evolve the system to the final state. The scheme is first-order implicit in the time domain (Li & Chen, 2019), and uses an explicit second-order finite difference scheme (Hu et al., 2012) for diffusion. We start at a small time step dt = 10^{-10} s, and gradually increase it to a tenth of the dynamic time scale ($\sim 10^{-4}$ s). A fixed mixing ratio of H_2, He, CH_4, C_2H_2, C_2H_4, and C_2H_6 are assumed at the lower boundary in accordance with number densities provided by (Moses & Poppe, 2017). We also maintain a zero flux boundary condition at the upper boundary, as atmospheric constituents are too heavy to escape. The narrow auroral arcs are 100 km long, and drift at a speed ~1 km/s (Achilleos et al., 2001). Thus, the time scale associated with electron precipitation can be estimated to be ~100 s.

2.4. Microwave Opacity of Jupiter's Upper Atmosphere

The presence of free electrons in a strongly collisional medium is analogous to those observed in Earth's aurora (Mannucci et al., 2015), where high electron-ion/neutral collision frequencies of a similar nature to the Jovian atmosphere coupled with high electron density generate the microwave opacity that could explain the auroral cold spot phenomenon (Rogers et al., 2015). Utilizing the Appleton-Lassen (derived from Appleton-Hartree) equations by (Hargreaves, 1969; Rogers et al., 2015), microwave absorption due to electrons in a highly collisional medium can be expressed as:

$$A = \int \alpha(z)\, dl, \tag{3}$$

where A is the attenuation in dB, z represents the altitude above the 1 bar atmospheric pressure, l is the microwave absorption path which equals z if the path is vertical, and $\alpha(z)$ is the absorptivity at the altitude z expressed in dB/km, which can be calculated as:

$$\alpha(z) = 4.6 \times 10^{-5}\frac{N_e(z)\nu_e(z)}{\nu_e^2(z) + \omega^2}, \tag{4}$$

where $N_e(z)$ is the altitude-dependent electron density per cubic meter. ν_e(z) is the combined electron-ion and electron-neutral collision frequency dependent on altitude, and ω is the microwave's angular frequency. We take into account collisions with H_2 (Pinto & Galli, 2008), He (Banks, 1966) and CH_4 (Song et al., 2015) to estimate total collision frequency.

In our plasma microwave opacity model, we assume that the ionosphere consists of multiple isothermal plasma layers characterized by elevated electron densities owing to electron precipitation. The relation between attenuation and brightness temperature is expressed as:

$$t_1 = 10^{-\frac{A}{10}}, \tag{5}$$

$$T_B = t_1 \times T_b + (1 - t_1) \times T_e, \tag{6}$$

where A is the attenuation in dB, t_1 is the transmissivity within the absorbing layer, T_B is the attenuated auroral brightness temperature emitted from the absorptive layer, T_b is the auroral brightness temperature from the layer below with the global average atmospheric brightness temperature as the T_b below the lowest absorbing layer, T_e is the ionospheric electron temperature. Figure 1 shows the list of models, and their corresponding inputs and outputs connected in their order of application.

3. Results

3.1. Juno MWR Observations

Figure 2 shows the range of T_A magnitudes for each PJ where T_A is expected to be less than the cutoff value. We set cutoff values for the 0.6 GHz channel, and the 1.2 GHz channel equal to 800 K, and 450 K respectively based on the probability distribution of T_A from atmospheric thermal radiation. It can be seen that regions of cold T_A have been observed over multiple orbits (Hodges et al., 2020). provided a detailed analysis of these cold regions during Juno's first 21 orbits. It represents the variation over various latitudes and footprint sizes. During the mission, the perijove of Juno continuously precessed northward, providing increased resolution of the northern high latitudes. Therefore, the MWR footprint over the North Pole varies over each perijove. Radiometer resolution is limited by the footprint length scale, and any variations in T_A can be partially attributed to the observation geometry, and distance from nadir view.

The footprint size is proportional to radial distance between Jupiter's microwave observational surface and the Juno spacecraft. As a result, the fraction of the MWR antenna beam that is filled by the auroral region changes from perijove to perijove and along the trajectory within each perijove, diluting the effect of the precipitating electrons by differing amounts on timescales from minutes to months.

We highlight the MWR observations corresponding to two distinct orbital geometries, that is, PJ 15 and PJ 22. These observations represent changes in MWR observation geometry and polar projection of antenna footprints. The footprint size decreases relative to the auroral oval in later PJ orbits as the mission evolves from PJ 15 to PJ 22 (Figures 3a and 3b).

These regions of cold T_A are primarily within the main auroral emission (MAE) and footprints of primary satellites: Io, Ganymede, and Europa. They are situated either poleward or in regions adjacent to the Io footprint. However, the morphology of cold regions can differ from one orbit to another (Bonfond et al., 2017). Provides the mean position of the MAE and satellite footprints over the North Pole. The footprint and MAE coordinates are publicly available in the supplementary data section of the referenced paper. During consecutive spacecraft spins, antenna footprints show a great degree of spatial overlap. Therefore, any change in T_A varying over Juno's spin period (~30 s) can be inferred to be emanating from similar spatial regions. They exhibit extreme changes between low and high T_A magnitudes mapped to be present during consecutive spins. Thus, the extreme variation in T_A observed during PJ 15 and PJ 22 polar passes can be attributed to short-time variations within the auroral ionospheric medium. T_A is expected to change within a spin period (~30 s). There is a 120° along-spin separation between the 0.6 GHz antenna boresight and the 1.2 GHz boresight, resulting in a 10 s delay between observations of the same location. As the stripes of high and low T_A regions do not show any spatial correlation between 0.6 and 1.2 GHz channels (Figures 3c–3f), the source function of the electrons absorbing the microwave emission can

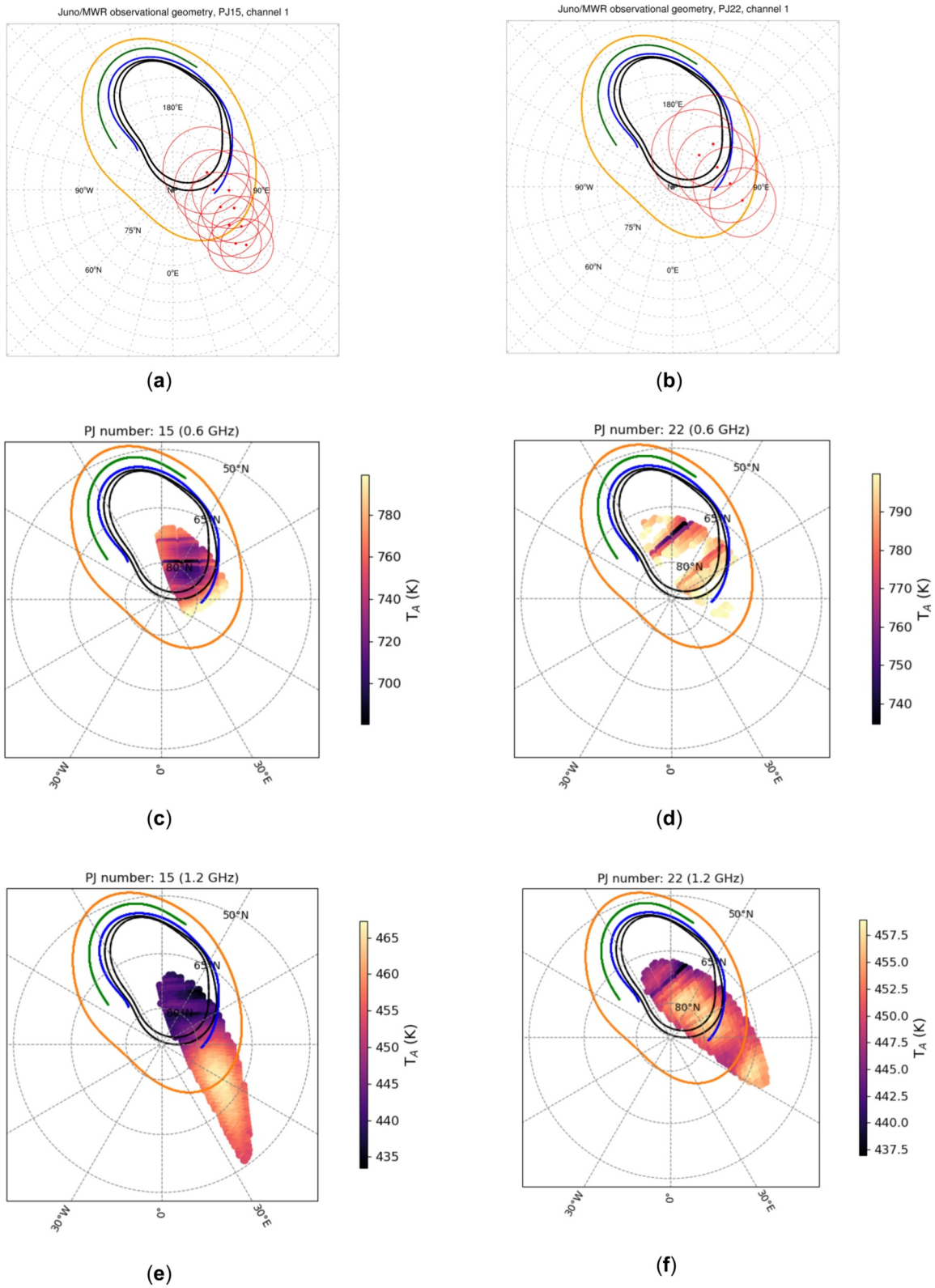

Juno/MWR observational geometry, PJ15, channel 1
Juno/MWR observational geometry, PJ22, channel 1
(a)
(b)
PJ number: 15 (0.6 GHz)
PJ number: 22 (0.6 GHz)
(c)
(d)
PJ number: 15 (1.2 GHz)
PJ number: 22 (1.2 GHz)
(e)
(f)
T_A (K)

Figure 3.

be expected to vary much faster (~10 s). This phenomenon has been clearly identified in other perijove orbits, including PJ 05, 10, 11, 16, 22, 26, 27, 28, 30, 32, 37, 40, 46 and 54.

3.2. High-Energy Electron Precipitation

The energy deposition of the JEDI-UVS composite electron spectrum peaks between 0.1 and 1 mbar pressure region, corresponding to altitudes between 150 and 250 km above the 1 bar level. We benchmark CSDA results with Planetocosmics (Desorgher et al., 2005), a Monte Carlo particle interaction model based on the GEANT4 (Agostinelli et al., 2003) framework (Figure 4a). Specifically, we use the implementation previously used by (Nordheim et al., 2015) to model particle precipitation at Venus, which has been recently adapted for Jupiter. Both CSDA, and Planetocosmics show agreement at higher energy bins corresponding to the peak in total energy deposition per volume amounting to 5×10^{-5} W/m^3. Compared to previous models, we expect electron density layers at lower altitudes (below CH_4 homopause).

About 18% of the total energy deposition undergoes excitation of atomic and molecular hydrogen at Lyman and Werner bands (Waite Jr et al., 1983). As electrons higher than 100–200 keV penetrate below the methane homopause, the auroral UV emission undergo atmospheric absorption due to H_2, He, CH_4 and C_2H_2. Estimating UV opacities for photoabsorption between 50 and 250 nm reveal sharp gradients in opacity. In the case of the PJ7 event, UV emission originating at 0.1 mbar level undergoes complete absorption between 70 and 125 nm as $\tau \sim 10^3$–10^6. At 1 μbar pressure, less than 1% of the total energy deposition may result in UV emissions as $\tau \sim 0.01$–1 between 110 and 125 nm wavelengths. Therefore, we find that UV auroral emissions may underestimate the population of high-energy electrons during extreme precipitation events.

3.3. Chemical Kinetics of Electron Precipitation

We solve the system of coupled chemical kinetic equations to estimate electron and ion concentrations corresponding to four cases of electron precipitation. JEDI and JEDI-UVS electron spectra distinguish the effects of electrons from 1 to 10 MeV. Two intermediate cases are generated by linearly scaling the JEDI-UVS intensities throughout the energy bins (Figure 5b). Electron densities build up to ~10^5–10^6 cm^{-3} within 100 s. This rapid increase in ionization also contributes to the formation of higher hydrocarbon ions like CH_5^+, and $C_2H_5^+$ that become dominant positive ions below the CH_4 homopause (Figures 5a–5c). The chemical pathways leading up to the formation of CH_5^+, $C_2H_5^+$ and heavier hydrocarbon ions by photoionization was developed previously (S. Atreya & T. Donahue, 1975; S. K. Atreya & Donahue, 1975; Y. Kim & Fox, 1994). This paper shows that energetic particle precipitation similarly results in the production of hydrocarbon ions at auroral latitudes. These ions and more complex hydrocarbon ions become dominant charge carriers below the CH_4 homopause (Drossart et al., 1993; Sinclair et al., 2017).

The penetration depth in the atmosphere is proportional to electron energy, therefore the extended energetic electron spectrum derived from UVS background counts contributes to additional ionization. Electron layers produced by energetic electrons are present much deeper compared to Galileo radio occultation derived ionospheric electron densities (Figure 5a) (Mendillo et al., 2022). This effect is also exhibited by hydrogen ions and we expect H_3^+ to dominate over H^+ below 400 km (Figure 5b). H_3^+ concentration is found to exist below 400 km alike the PJ 1 simulations of UV emission (Gérard et al., 2023).

3.4. Microwave Transmission in Jupiter's Upper Atmosphere

We run cases of monoenergetic electron beams to understand the sensitivity of microwave opacity to primary electron energies. Four cases of monoenergetic beams: 100, 300, 500, and 1,000 keV with intensity ~10 erg/cm^{2}s are simulated for secondary electron impact ionization for 100 s. Microwave absorptivity for electron density

Figure 3. Polar projections of MWR antenna footprints (channel 1–0.6 GHz), and antenna temperatures (0.6 and 1.2 GHz) corresponding to PJ orbits 15 (a), (c), (e) and 22 (b), (d), (f). The footprint size of the MWR antenna beam changes relative to size of the auroral oval (black), and the footprints of Io (orange), Europa (green), and Ganymede (blue). The plotted footprints represent a sample of actual footprints throughout the course of the mission. As the mission progresses the altitude of the observation changes due to the northward precession of the perijove of Juno's orbit. The low resolution of the low frequency channels show a large degree of overlap between consecutive spins. Consecutive spins observe the same region of atmosphere due to the overlapping footprints. Thus, rapid changes in T_A are associated with temporal changes in the ionospheric medium. The cold regions at 0.6 GHz are bounded by the Io footprint, and spatial variations of polar auroral emissions.

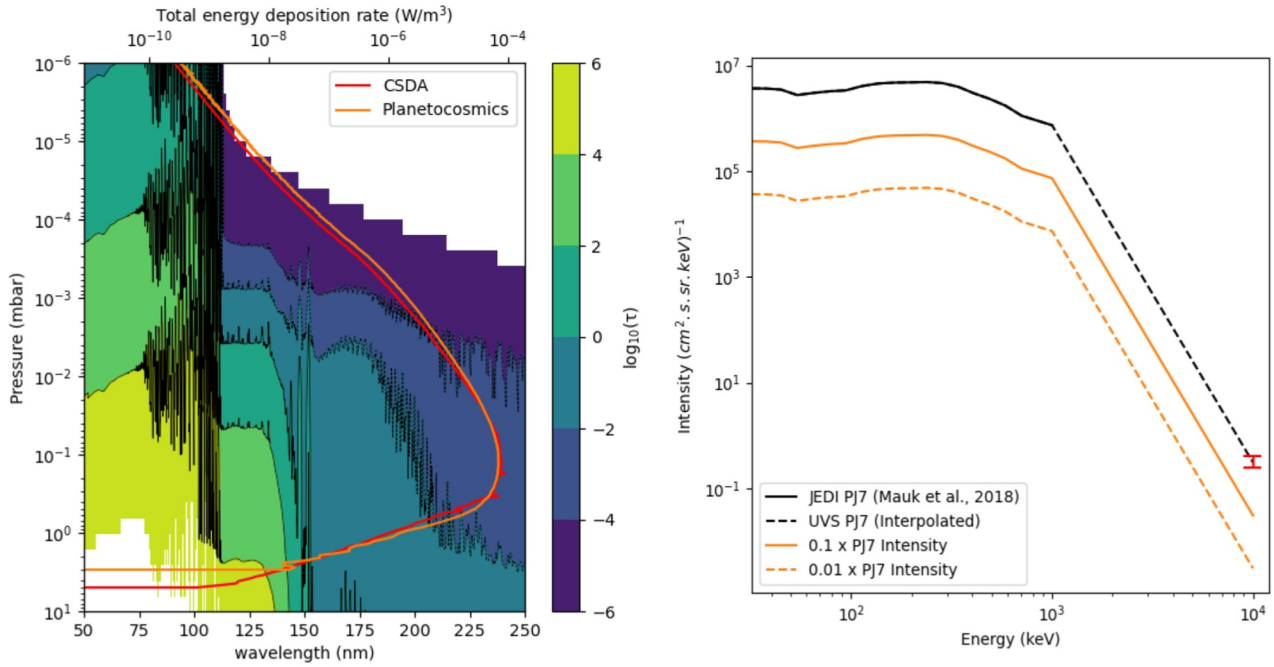


Figure 4. (a) Energy deposition rates computed by CSDA and Planetocosmics for high intensity downward precipitating electrons during PJ 7. Peak energy deposition is compared with atmospheric ultraviolet opacity for wavelengths ranging between 50 and 250 nm from H_2, He, CH_4 and C_2H_2 photon absorption. (b) Intensity of downward directed electrons as inferred from JEDI and UVS composite data. The red bar indicates the uncertainty bounds for 10 MeV energy intensity required to match the UVS background rate for integrated flux between 6 and 10 MeV. The 10 MeV intensity is interpolated with JEDI data to match the UVS background corresponding to 11 July 2017 at 01:14:38 UTC.

profiles are calculated based on the Appleton-Lassen theory described before. The microwave absorptivity shows a monotonic increase with electron beam energy due to an increase in penetration depth. The absorptivity profile at 1 MeV is 100 times larger than the 100 keV monoenergetic beam (Figures 6a–6d)). Therefore, the ionospheric microwave opacity is very sensitive to high-energy electrons (≥ 500 keV).

The interaction of free electrons with neutrals acts as a strongly collisional medium opaque to atmospheric microwave thermal emission from deeper levels. The brightness temperature observed by the Juno MWR instrument over these cold spots should be attributed to local electron temperature, and microwave absorption in the medium. Ionospheric electrons contribute to a wide range of microwave absorptivities for MWR (0.6–5.2 GHz). The intensity and energy of high-energy electrons affect the amount of microwave attenuation. This can be seen in the lower attenuation from cases where JEDI and UVS electron intensity is scaled by 0.1 and 0.01 to simulate intermediate particle precipitation events (Figures 7a–7d). Brightness temperature due to the auroral electron absorption A summary of total microwave attenuation caused by the four cases of electron precipitation events is provided in Table 1.

Due to their greater sensitivity to electron precipitation, the substantially higher attenuation in lower frequency channels (0.6 and 1.2 GHz) results in much lower brightness temperatures. For example, the attenuated brightness temperature (168.51 K) for JEDI and UVS condition in the 0.6 GHz channel is lower than the cold spot brightness temperature deconvolved from antenna temperature data from PJ7 (Hodges et al., 2020). This discrepancy could be potentially explained by the electron precipitation events being temporary and spatially limited to a size smaller than the MWR's 0.6 and 1.2 GHz channel footprint projection during the main phase orbits, resulting in the Juno MWR antenna receiving both the partially attenuated and unattenuated brightness temperature data within the cold spots. Electron impact processes can lead to near-complete or complete absorption of thermal radiation (Table 1) in the atmospheric region within the precipitating electron beam.

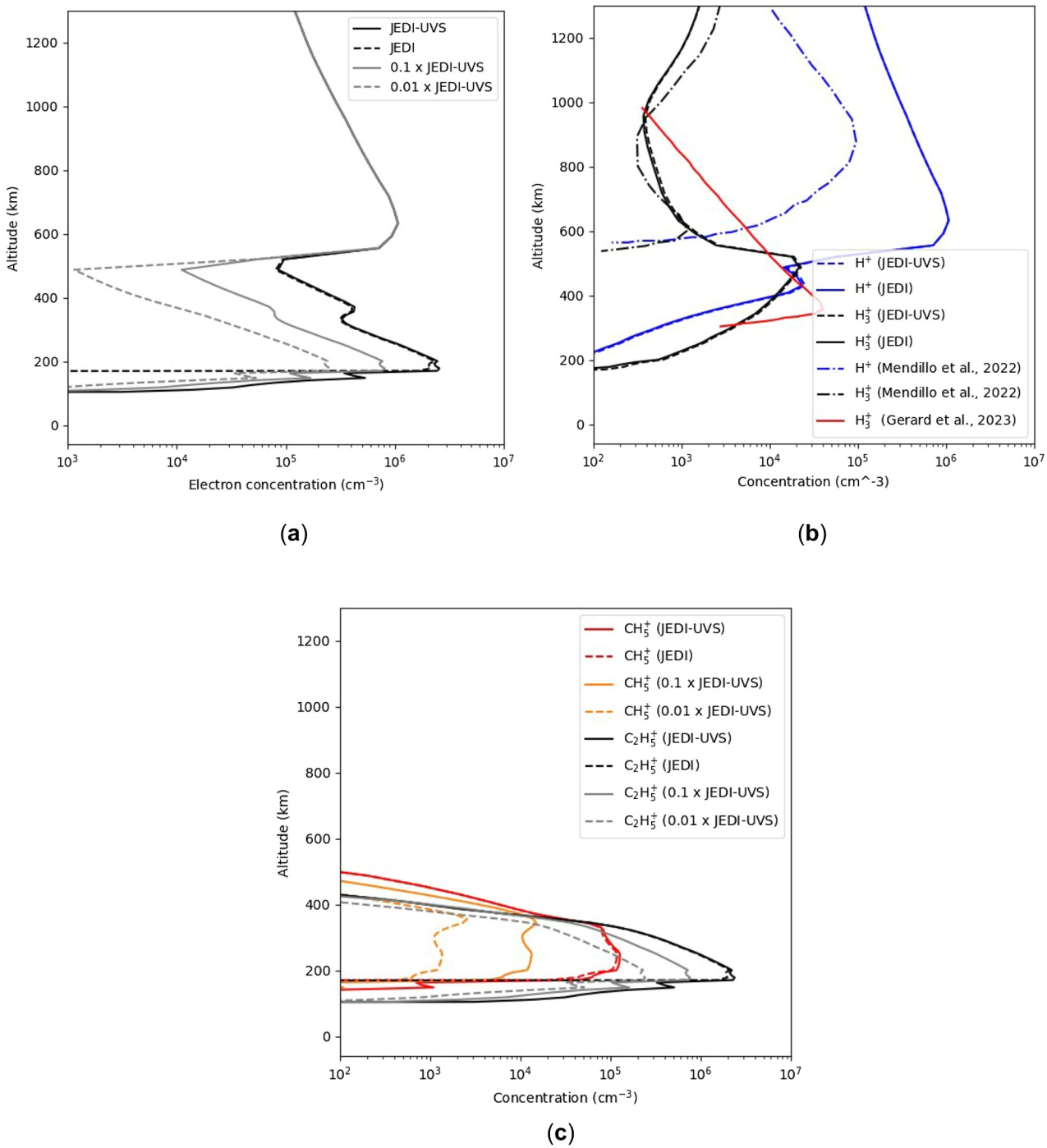


Figure 5. Concentrations of key neutrals, ions, and electrons in Jupiter's upper atmosphere corresponding to four cases of PJ 7 event for a duration of 100 s. (a) Auroral ionospheric electron concentration (cm^{-3}), (b) hydrogen ion concentrations (H^+ and H_3^+) compared to low latitude ionosphere and PJ 1 simulation, (c) auroral hydrocarbon ion concentrations (CH_5^+ and $C_2H_5^+$) due to high-energy electron precipiation.

The effective antenna temperature can be expressed as a sum of contributions from the ionosphere and deep thermal emission averaged over its areas. The variation in spatial scales associated with high-energy electron beams directly affects the contributions of the auroral ionosphere. Here we introduce the concept of fill factor that is, ratio of projected electron beam area to that of MWR footprint. The fill factor determines the contribution of auroral electrons to the boresight temperature. Based on the estimated antenna temperature (Table 1) from

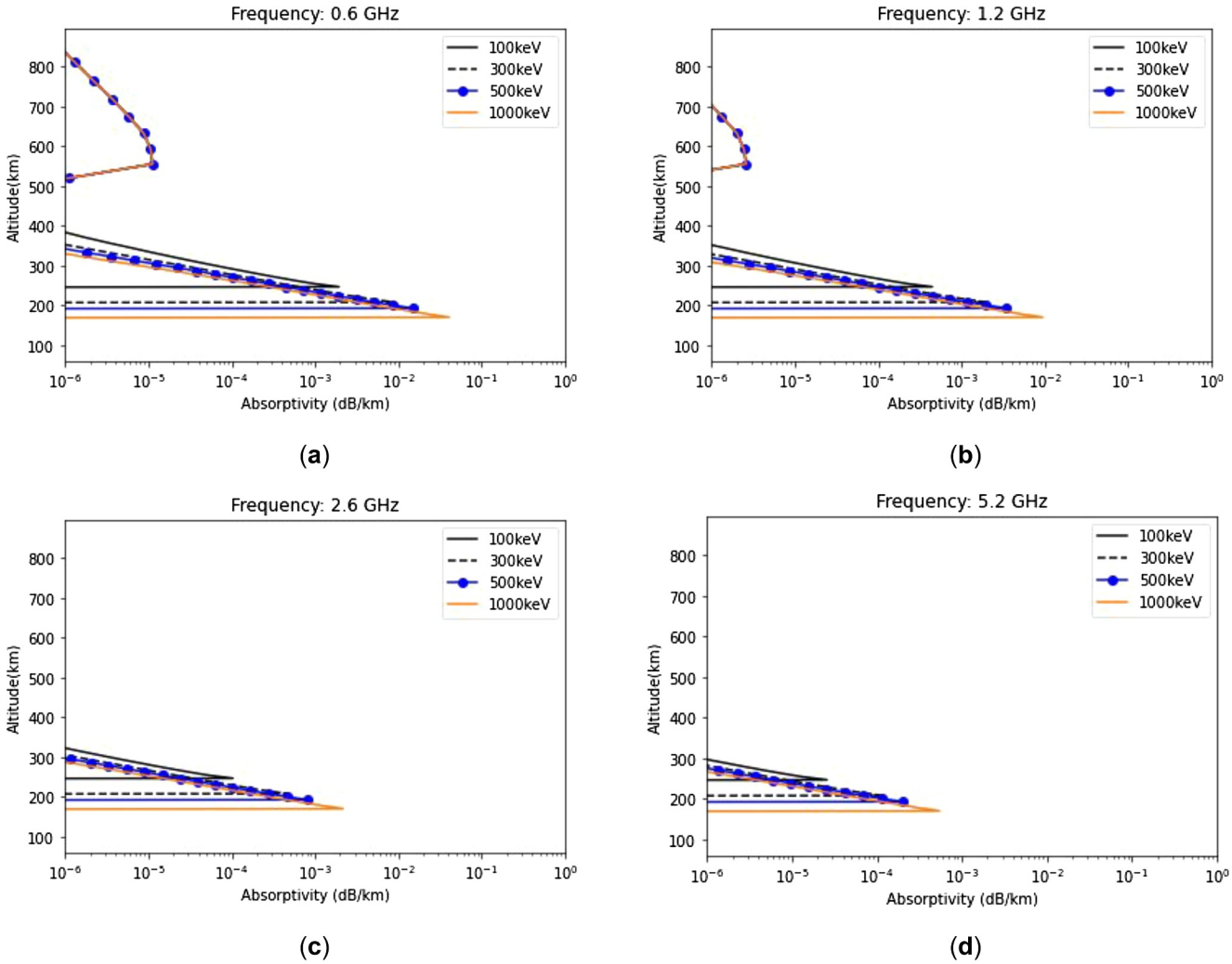


Figure 6. Microwave absorptivity (dB/km) for photochemically generated ionosphere, and four cases of the monoenergetic electron beam at the four lowest frequency MWR channels that is, (a) 0.6, (b) 1.25, (c) 2.6, and (d) 5.2 GHz.

different cases of electron precipitation, we determine the possible fill factors required to explain the antenna temperatures for the first two frequency channels (0.6 and 1.2 GHz).

$$T_{eff} = f \times T_B + (1 - f) \times T_{th}, \tag{7}$$

Here, T_{eff} is effective footprint averaged temperature, T_{th} is brightness temperature corresponding to atmospheric thermal emission and f is the fill factor. The analysis of the first two frequency channels reveals electron beams to cover ~7 to 80% of the MWR footprint area (Figure 8). We assume MWR channel footprint size ~0.1 R_j for our calculations, consistent with MWR footprint geometry.

The electron beam scale from the JEDI in-situ field of view (FOV) is estimated from the orbital speed of Juno from the radial position of the spacecraft. Spacecraft passes over the northern aurora and polar cap have identified several events associated with a high flux of downward precipitation electrons. During PJ1, PJ5, and PJ10 we find that high-energy electron intensities can rise up to magnitudes corresponding to PJ7 and associated down-scaled energy spectra (Figure 4b). Table 2 summarizes the peak energy, intensity, and time scale associated with the high-energy electron flux events. For detailed information about electron energy and pitch angle distributions, one can refer to the previous literature on JEDI observations (B. H. Mauk et al., 2017; B. Mauk et al., 2018; Clark et al., 2018; B. H. Mauk et al., 2020).

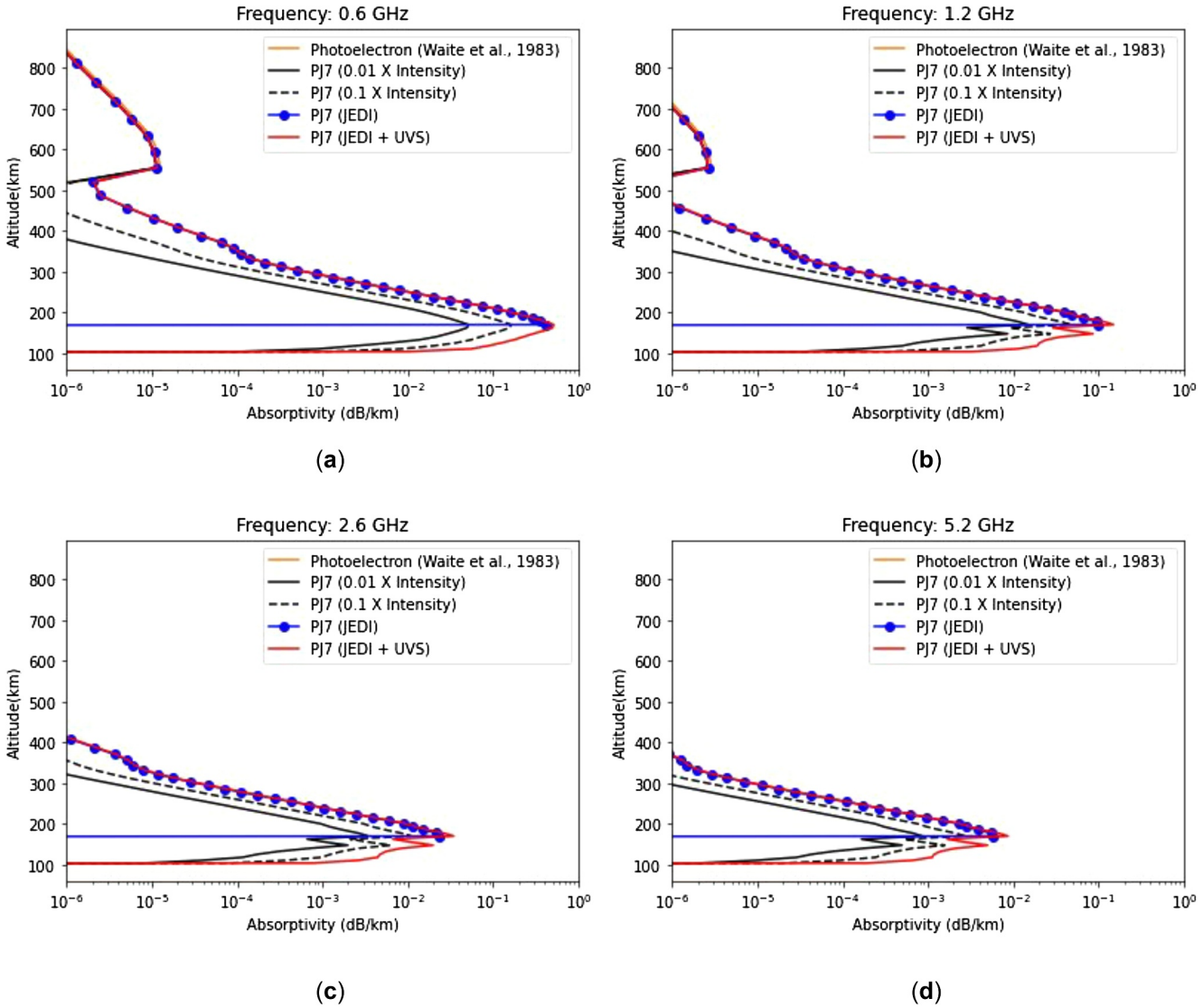


Figure 7. Microwave absorptivity (dB/km) for photochemically generated ionosphere, and four cases of PJ 7 precipitation event at the four lowest frequency channels that is, (a) 0.6, (b) 1.25, (c) 2.6, and (d) 5.2 GHz. The photochemically generated ionosphere doesn't contribute significant attenuation to atmospheric thermal radiation. However, energetic precipitation events such as the PJ7 event modeled herein can cause intermediate to near-complete absorption of microwave radiation with a decrease in the magnitude of attenuation with increasing microwave frequency. At altitudes below 100 km (4 mbar) and above 1,200 km (0.1 nbar), microwave absorption from electrons becomes insignificant due to insufficient electron densities.

Table 1
Microwave Attenuation a and Attenuated Brightness Temperature T_B at Nadir View of the Ionospheric Medium Subject to Electron Precipitation at Different Intensities

Condition	JEDI and UVS	JEDI	JEDI and UVS electron intensity scaled by 0.1	JEDI and UVS electron intensity scaled by 0.01	Photoelectrons
$A_{0.6GHz}$	28.65 dB	13.27 dB	8.87 dB	2.68 dB	0.0021 dB
$T_{B,\,0.6GHz}$	167.29 K	198.15 K	253.46 K	530.1 K	841.06 K
$A_{1.25GHz}$	5.93 dB	3.19 dB	1.82 dB	0.55 dB	0.00048 dB
$T_{B,\,1.25GHz}$	238.63 K	302.96 K	353.50 K	417.70 K	451.63 K
$A_{2.6GHz}$	1.37 dB	0.74 dB	0.42 dB	0.13 dB	0.00011 dB
$T_{B,\,2.6GHz}$	282.45 K	300.90 K	311.06 K	321.30 K	325.91 K
$A_{5.2GHz}$	0.34 dB	0.18 dB	0.11 dB	0.032 dB	2.8×10^{-5} dB
$T_{B,\,5.2GHz}$	238.59 K	241.32 K	242.70 K	244.03 K	244.60 K

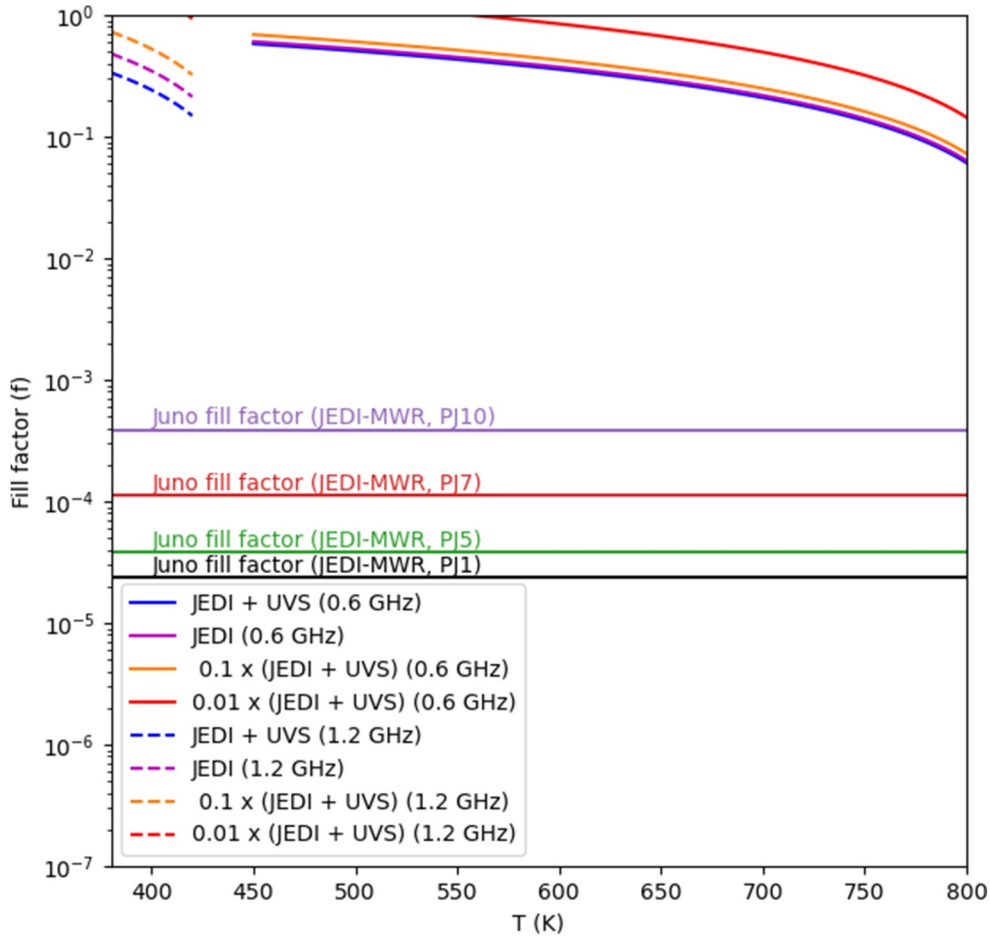


Figure 8. Fill factor inferred from MWR cold spot antenna temperatures for different cases of high-energy electron precipitation. MWR fill factors for 0.6 and 1.2 GHz frequency channels range between 7 and 80 assuming a MWR footprint size ~0.1 R_j. The JEDI in-situ precipitation region is found to be two orders of magnitude smaller than that inferred from model solutions. We identify fill factors corresponding to JEDI downward electron flux data over north pole collected during PJ1, PJ5, PJ7, and PJ10. Thus, cold spot antenna temperatures are found to be highly sensitive to electron beam spatial scales to the peak energy of the electrons and to the energy flux of the electrons.

Orbital speed and event time scales determine the length scale of these downward-directed energetic electron flux events from JEDI FOV. It is compared against the MWR antenna footprint size to estimate fill factors. JEDI FOV based fill factors are found to be much smaller than predictions from different cases of electron precipitation. This effect can be attributed to limited global scale coverage of electron precipitation over the north pole and rapid changes associated with electron beam intensities. High-energy electron beams are quite ubiquitous as inferred from UVS color ratio (Benmahi et al., 2024) and statistical analysis of JEDI electron beams (Salveter et al., 2022). However, the penetration of secondary electrons at greater depths causes a large proportion of UV emissions to be absorbed by the atmospheric column above (Figure 4a).

Table 2
High-Energy Electron Flux Events Reported From JEDI Observations

PJ	Radius (R_j)	Time (s)	Peak energy	Peak flux (1/cm^2 s sr keV)	Reference
1	1.5	1	Broadband event	10^6	(B. Mauk et al., 2017)
5	1.3	1.5	Broadband event	10^6	(Ebert et al., 2019)
7	1.64	5	300 keV	Between 10^6–10^7	(B. H. Mauk et al., 2020)
10	2.21	20	500–700 keV	10^6	(B. H. Mauk et al., 2020)

Table 3
ASummary of Factors Responsible for Variations in MWR Antenna Temperatures Over Jupiter's Northern Aurora

Cause	Methodology	Conclusion
Variation in intensity and energy of downward directed electron flux	Calculate microwave absorptivity profile and brightness temperatures for different electron beam intensities and energy distributions	0.6 GHz channel auroral T_B vary between 168.23–556.50 K 1.2 GHz channel auroral T_B vary between 238.63–302.96 K
Variation in spatial scales of downward directed electrons	Calculate fill factors based on MWR antenna temperatures and apriori knowledge of brightness temperature contributions from aurora and deep thermal emission	Fill factors range between 7% and 80% of MWR footprint area
Variation in MWR footprint size relative to aurora (fill factor)	Normalize antenna temperatures to square of radial distance to spacecraft expressed in R_j	Unnormalized 0.6 GHz channel T_A vary between 450–800 K Unnormalized 1.2 GHz channel T_A vary between 350–450 K Footprint size proportional to radial distance between Juno spacecraft and Jupiter

4. Discussion and Summary

Electron precipitation has profound effects on Jupiter's auroral ionosphere. Juno energetic particle instruments have provided a comprehensive survey of energetic electrons beaming into the atmosphere. By using an electron precipitation event during PJ 7 representative of the newly discovered (B. Mauk et al., 2018) extreme precipitation events, we have estimated consequences due to collisional interaction between precipitating electrons and neutral molecules. Electrons with energies larger than 100 keV will penetrate deeper than the methane homopause (Egert et al., 2017). Electron impact ionization at deeper levels initiates a chain of reactions leading to the formation of short-lived hydrocarbon ions. It is established through modeling and simulation that a short-time scale event (~ 100 s) can provide appreciable microwave absorption required to explain cold features inferred from MWR, while at the same time resulting in absorption of the ultraviolet H_2 band emissions below 150 nm. The CH_4 and C_2H_2 absorption bands above 150 nm allow UV emission transmission, leading to a high UV color ratio. The UV color ratio represented as the ratio of UV emission intensities between 155–162 nm and 123–130 nm bands. It is used as a measure of the precipitating energetic particle flux (due to their depth of penetration into the atmospheric column). Near-complete absorption of low wavelength UV flux intensity from deeper levels causes them to be sensitive to UV emission at shallow levels contributed by low energy electrons.

The sporadic nature of precipitation intensities can explain the temporal variations in the high-latitude ionosphere. The hydrocarbon ions will undergo rapid dissociative recombination with ionospheric electrons. Recombination coefficients (α_r) for the major hydrocarbon ions are $\sim 5 \times 10^{-7}$ cm^3/s. With an electron density (N_e) in the range of 10^5–10^6 cm^{-3}, the hydrocarbon ion recombination time scale, $\tau_r \sim \frac{1}{\alpha_r N_e} \sim$ 2–20 s.

The antenna temperatures observed at 0.6 and 1.2 GHz channels can be attributed to a combination of three factors. First, the intensity and energy of downward-directed electrons that directly affect microwave opacity and ionospheric free electron concentration. Second, the spatial scales associated with electron precipitation within the MWR footprint influence the boresight antenna temperature. Finally, the change in MWR antenna footprint size over Juno orbits introduces additional variations in antenna temperature due to the contribution of both thermal and non-thermal sources to the observed antenna temperatures within the beam shape (Table 3).

Our analysis shows MWR cold spots exhibit a large range of T_A values at 0.6 GHz (450–850 K) and 1.2 GHz (350–450 K) channels for the first 54 Juno orbits. High-energy electrons measured by the JEDI instrument contribute to transient enhancements in local electron densities in the lower stratosphere. We determine that high-energy electrons can contribute anywhere between 2.38 and 25.66 dB loss in microwave transmission, leading to partial or near-complete absorption of Jupiter's thermal emission. The change in MWR antenna beam shape and its relative position to the main auroral oval are equally important contributing factors to the cold spot T_A values. The local ionospheric medium exhibits rapid changes in T_A within Juno spin period of 30 s due to competing ionization and dissociative recombination processes. A PJ 7 like extreme electron precipitation event produces UV emission at Lyman and Werner bands that undergo complete absorption below 150 nm. Thus, microwave

observations of Jupiter's Northern Aurora can complement the UV emission observations to understand high-energy electron precipitation and atmospheric ionization process.

Appendix A: Chemical Reactions and Rate Expressions

The list of all chemical reactions associated with Jupiter's electron precipitation model are summarized in this section. The list of chemical reactions corresponding to Jupiter's ionosphere can be grouped into several categories that is, electron impact ionization, bimolecular reactions, three-body reactions, and vibrational excitation and exchange processes.

Table A1
List of Electron Impact Processes

Index	Equation
E_1	$H_2 + e_{cr}^- \rightarrow H_2^+ + e^- + e_{cr}^-$
E_2	$H_2 + e_{cr}^- \rightarrow H^+ + H + e^- + e_{cr}^-$

Table A2
List of Ion-Neutral and Electron Recombination Reactions

Index	Equation	k	Rate expression
C_1	$H + CH \rightarrow C + H_2$	$a = 1.4 \times 10^{-11}$, $b = 0.0$, $E_a = 0.0$	(Becker et al., 1989)
C_2	$H + {}^1CH_2 \rightarrow CH + H_2$	$a = 2.0 \times 10^{-10}$, $b = 0.0$, $E_a = 0.0$	(Brownsword et al., 1997)
C_2	$H + {}^3CH_2 \rightarrow CH + H_2$	$a = 2.66 \times 10^{-10}$, $b = 0.0$, $E_a = 0.0$	(Canosa et al., 1997)
C_3	$H + CH_3 \rightarrow {}^1CH_2 + H_2$	$a = 1.0 \times 10^{-10}$, $b = 0.0$, $E_a = 7{,}600.0$	(Perry et al., 1999)
C_4	$H + CH_4 \rightarrow CH_3 + H_2$	$a = 3.73 \times 10^{-20}$, $b = 3.0$, $E_a = 4{,}406.0$	(Perry et al., 1999)
C_5	$H + C_2H_3 \rightarrow C_2H_2 + H_2$	$a = 2.0 \times 10^{-11}$, $b = 0.0$, $E_a = 0.0$	(Baulch et al., 1994)
C_6	$H + C_2H_4 \rightarrow C_2H_3 + H_2$	$a = 9.0 \times 10^{-10}$, $b = 0.0$, $E_a = 7{,}500.0$	(Perry et al., 1999)
C_7	$H + C_2H_6 \rightarrow C_2H_5 + H_2$	$a = 2.35 \times 10^{-15}$, $b = -1.5$, $E_a = 3{,}725.0$	(Baulch et al., 1992)
C_8	$H_2 + CH \rightarrow {}^3CH_2 + H$	$a = 3.1 \times 10^{-10}$, $b = 0.0$, $E_a = 1{,}650.0$	(Brownsword et al., 1997)
C_9	$H_2 + {}^1CH_2 \rightarrow CH_3 + H$	$a = 9.24 \times 10^{-11}$, $b = 0.0$, $E_a = 0.0$	(Yung et al., 1984)
C_{10}	$H_2 + {}^1CH_2 \rightarrow {}^3CH_2 + H_2$	$a = 1.26 \times 10^{-11}$, $b = 0.0$, $E_a = 0.0$	(Yung et al., 1984)
C_{11}	$H_2 + CH_3 \rightarrow CH_4 + H$	$a = 1.14 \times 10^{-20}$, $b = 2.74$, $E_a = 4{,}740.0$	(Baulch et al., 1992; Perry et al., 1999)
C_{12}	$H_2 + C_2H_3 \rightarrow C_2H_4 + H$	$a = 5.0 \times 10^{-20}$, $b = 2.63$, $E_a = 4{,}298.0$	(Fahr & Laufer, 1995)
C_9	$CH + CH_4 \rightarrow C_2H_4 + H$	$a = 3.96 \times 10^{-8}$, $b = -1.04$, $E_a = 36.1$	(Canosa et al., 1997)
C_{13}	$CH + C_2H_4 \rightarrow C_2H_2 + CH_3$	$a = 2.23 \times 10^{-10}$, $b = 0.0$, $E_a = -173.0$	(Berman et al., 1982)
C_{14}	$CH + C_2H_6 \rightarrow C_2H_4 + CH_3$	$a = 1.9 \times 10^{-8}$, $b = -0.859$, $E_a = 53.2$	(Canosa et al., 1997)
C_{15}	$2\ {}^3CH_2 \rightarrow C_2H_2 + H_2$	$a = 2.0 \times 10^{-11}$, $b = 0.0$, $E_a = 400.0$	(Baulch et al., 1992)
C_{16}	$2\ {}^3CH_2 \rightarrow C_2H_2 + 2\ H$	$a = 1.8 \times 10^{-11}$, $b = 0.0$, $E_a = 400.0$	(Baulch et al., 1992)
C_{17}	${}^3CH_2 + C_2H_3 \rightarrow C_2H_2 + CH_3$	$a = 8.0 \times 10^{-11}$, $b = 0.0$, $E_a = 0.0$	(Moses et al., 2004)
C_{18}	${}^1CH_2 + CH_4 \rightarrow CH_4 + {}^3CH_2$	$a = 1.2 \times 10^{-11}$, $b = 0.0$, $E_a = 0.0$	(Böhland et al., 1985)
C_{20}	$2\ CH_3 \rightarrow C_2H_5 + H$	$a = 5.0 \times 10^{-11}$, $b = 0.0$, $E_a = 6{,}800.0$	(Baulch et al., 1992; Perry et al., 1999)
C_{21}	$CH_3 + C_2H_3 \rightarrow C_2H_2 + CH_4$	$a = 3.4 \times 10^{-11}$, $b = 0.0$, $E_a = 0.0$	(Fahr et al., 1991)
C_{22}	$CH_3 + C_2H_4 \rightarrow C_2H_3 + CH_4$	$a = 6.9 \times 10^{-11}$, $b = 0.0$, $E_a = 5{,}600.0$	(Baulch et al., 1992; Perry et al., 1999)
C_{23}	$CH_3 + C_2H_6 \rightarrow C_2H_5 + CH_4$	$a = 2.45 \times 10^{-31}$, $b = 6.0$, $E_a = 3{,}043.0$	(Baulch et al., 1992; Perry et al., 1999)
C_{24}	$C_2H_5 + H \rightarrow 2\ CH_3$	$a = 1.25 \times 10^{-10}$, $b = 0.0$, $E_a = 0.0$	(Moses et al., 2000)
C_{25}	$C_2H_5 + H \rightarrow C_2H_4 + H_2$	$a = 3.0 \times 10^{-12}$, $b = 0.0$, $E_a = 0.0$	(Moses et al., 2000)

Table A3
List of Three-Body Reactions

Index	Equation	k_0	k_∞	Rate expression
T_1	$H + CH_3$ (+M) → CH_4 (+M)	$a = 5.8 \times 10^{-29}$, $b = 0.0$, $E_a = -355.0$	$a = 2.37 \times 10^{-12}$, $b = 0.0$, $E_a = -523.0$	(Allen et al., 1992)
T_2	$H + {}^3CH_2$ (+M) → CH_3 (+M)	$a = 5.8 \times 10^{-30}$, $b = 0.0$, $E_a = -355.0$	$a = 2.37 \times 10^{-12}$, $b = 0.0$, $E_a = -523.0$	(G. R. Gladstone et al., 1996)
T_3	$H + C_2H_2$ (+M) → C_2H_3 (+M)	$a = 2.6 \times 10^{-31}$, $b = 0.0$, $E_a = 0.0$	$a = 3.8 \times 10^{-11}$, $b = 0.0$, $E_a = 1{,}374.0$	(Romani et al., 1993)
T_4	$H + C_2H_3$ (+M) → $C_2H_2 + H_2$ (+M)	$a = 1.49 \times 10^{-27}$, $b = 0.0$, $E_a = 0.0$	$a = 1.55 \times 10^{-10}$, $b = 0.0$, $E_a = 0.0$	(Romani, 1996)
T_5	$H + C_2H_4$ (+M) → C_2H_5 (+M)	$a = 2.15 \times 10^{-29}$, $b = 0.0$, $E_a = 349.0$	$a = 4.95 \times 10^{-11}$, $b = 0.0$, $E_a = 1{,}051.0$	(Romani et al., 1993)
T_6	$H_2 + CH$ (+M) → CH_3 (+M)	$a = 4.7 \times 10^{-26}$, $T_0 = 1$, $b = -1.6$, $E_a = 0.0$	$a = 2.5 \times 10^{-10}$, $T_0 = 1$, $b = -0.08$, $E_a = 0.0$	(Brownsword et al., 1997)
T_7	$H_2 + CH + M$ → ${}^1CH_2 + H + M$	$a = 2.38 \times 10^{-11}$, $T_0 = 1$, $b = 0.0$, $E_a = 1{,}760.0$	-	(Yung et al., 1984)
T_8	$H_2 + C_2H_3 + M$ → $C_2H_4 + H + M$	$a = 5.0 \times 10^{-20}$, $T_0 = 1$, $b = 2.63$, $E_a = 4{,}298.0$	-	(Romani, 1996)
T_9	$CH + CH_4 + M$ → $C_2H_4 + H + M$	$a = 2.5 \times 10^{-11}$, $b = 0.0$, $E_a = 200.0$	-	(Yung et al., 1984)
T_{10}	2 CH_3 (+M) → C_2H_6 (+M)	$a = 2.22 \times 10^{-16}$, $T_0 = 1$, $b = -3.75$, $E_a = 494.0$	$a = 3.78 \times 10^{-9}$, $T_0 = 1$, $b = -0.69$, $E_a = 88.0$	(Wang et al., 2003)
T_{11}	$CH_3 + C_2H_3 + M \rightarrow C_3H_6 + M$	$a = 1.1 \times 10^{-28}$, $T_0 = 1$, $b = 8.52$, $E_a = -1{,}248.0$	-	(G. R. Gladstone et al., 1996)
T_{12}	$C + H_2 + M \rightarrow {}^3CH_2$	$a = 7.0 \times 10^{-32}$, $T_0 = 1$, $b = 0.0$, $E_a = 0.0$	$a = 2.06 \times 10^{-11}$, $T_0 = 1$, $b = 0.0$, $E_a = 57.0$	(Moses et al., 2000)
T_{13}	2 $C_2H_3 + M$ → $C_2H_4 + C_2H_2 + M$	$a = 2.4 \times 10^{-11}$, $b = 0.0$, $E_a = 0.0$	-	(Yung et al., 1984)
T_{14}	$2 H + M \rightarrow H_2 + M$	$a = 2.7 \times 10^{-31}$, $T_0 = 1$, $b = -0.6$, $E_a = 0.0$	-	(Baulch et al., 1992; Perry et al., 1999)

Table A4
List of Ion-Neutral and Electron Recombination Reactions

Index	Equation	k	Rate expression
C_1	$H_2^+ + H_2 \rightarrow H_3^+ + H$	$a = 1.72 \times 10^{-9}$, $b = 0.0$, $E_a = 0.0$	(Miller et al., 1968)
C_2	$H_2^+ + e^- \rightarrow 2 H$	$a = 2.25 \times 10^{-6}$, $T_0 = 1$, $b = -0.4$, $E_a = 0.0$	(Mitchell, 1990)
C_3	$H_3^+ + e^- \rightarrow H_2 + H$	$a = 4.932 \times 10^{-8}$, $T_0 = 300$, $b = -1.0$, $E_a = 0.0$	(Glosik et al., 2005; McCall et al., 2004)
C_4	$H_3^+ + e^- \rightarrow 3 H$	$a = 8.768 \times 10^{-8}$, $T_0 = 300$, $b = -1.0$, $E_a = 0.0$	(Glosik et al., 2005; McCall et al., 2004)
C_5	$H_3^+ + He \rightarrow HeH^+ + H_2$	$a = 3.0 \times 10^{-12}$, $b = 0.0$, $E_a = 0.0$	(Aquilanti et al., 1965)
C_6	$H_2^+ + H \rightarrow H^+ + H_2$	$a = 6.4 \times 10^{-10}$, $b = 0.0$, $E_a = 0.0$	(V. Anicich et al., 1979)
C_7	$H^+ + CH_4 \rightarrow CH_3^+ + H_2$	$a = 3.403 \times 10^{-9}$, $b = 0.0$, $E_a = 0.0$	(V. G. Anicich, 1993)
C_8	$H^+ + CH_4 \rightarrow CH_4^+ + H$	$a = 7.47 \times 10^{-10}$, $b = 0.0$, $E_a = 0.0$	(V. G. Anicich, 1993)
C_9	$H_3^+ + CH_4 \rightarrow CH_5^+ + H_2$	$a = 2.4 \times 10^{-9}$, $b = 0.0$, $E_a = 0.0$	(Praxmarer et al., 1994)
C_{10}	$H^+ + e^- \rightarrow H$	$a = 1.66 \times 10^{-10}$, $T_0 = 1$, $b = -0.64$, $E_a = 0.0$	(Millar et al., 1997)
C_{11}	$H_2^+ + CH_4 \rightarrow CH_5^+ + H$	$a = 1.1 \times 10^{-10}$, $b = 0.0$, $E_a = 0.0$	(J. Kim & Huntress, 1975)
C_{12}	$H_2^+ + CH_4 \rightarrow CH_4^+ + H_2$	$a = 1.41 \times 10^{-9}$, $b = 0.0$, $E_a = 0.0$	(J. Kim & Huntress, 1975)
C_{13}	$H_2^+ + CH_4 \rightarrow CH_3^+ + H + H_2$	$a = 2.28 \times 10^{-9}$, $b = 0.0$, $E_a = 0.0$	(J. Kim & Huntress, 1975)
C_{14}	$CH_4^+ + e^- \rightarrow CH_3 + H$	$a = 6.09 \times 10^{-8}$, $T_0 = 300$, $b = -0.53$, $E_a = 0.0$	(Sheehan & Maurice, 2004; Reiter & Janev, 2010)
C_{15}	$CH_4^+ + e^- \rightarrow CH_2 + 2 H$	$a = 1.247 \times 10^{-7}$, $T_0 = 300$, $b = -0.53$, $E_a = 0.0$	(Sheehan & Maurice, 2004; Reiter & Janev, 2010)
C_{16}	$CH_4^+ + e^- \rightarrow CH_2 + H_2$	$a = 2.61 \times 10^{-8}$, $T_0 = 300$, $b = -0.53$, $E_a = 0.0$	(Sheehan & Maurice, 2004; Reiter & Janev, 2010)
C_{17}	$CH_4^+ + e^- \rightarrow CH + H_2 + H$	$a = 7.25 \times 10^{-8}$, $T_0 = 300$, $b = -0.53$, $E_a = 0.0$	(Sheehan & Maurice, 2004; Reiter & Janev, 2010)

Table A4
Continued

Index	Equation	k	Rate expression
C_{18}	$CH_4^+ + e^- \rightarrow C + 2\,H_2$	$a = 5.8 \times 10^{-9}$, $T_0 = 300$, $b = -0.53$, $E_a = 0.0$	(Sheehan & Maurice, 2004; Reiter & Janev, 2010)
C_{19}	$CH_5^+ + e^- \rightarrow CH_4 + H$	$a = 1.45 \times 10^{-8}$, $T_0 = 300$, $b = -0.46$, $E_a = 0.0$	(Semaniak et al., 1998; Sheehan & Maurice, 2004)
C_{20}	$CH_5^+ + e^- \rightarrow CH_3 + H_2$	$a = 1.45 \times 10^{-8}$, $T_0 = 300$, $b = -0.46$, $E_a = 0.0$	(Semaniak et al., 1998; Sheehan & Maurice, 2004)
C_{21}	$CH_5^+ + e^- \rightarrow CH_3 + 2\,H$	$a = 2.03 \times 10^{-7}$, $T_0 = 300$, $b = -0.46$, $E_a = 0.0$	(Semaniak et al., 1998; Sheehan & Maurice, 2004)
C_{22}	$CH_5^+ + e^- \rightarrow CH_2 + H_2 + H$	$a = 5.22 \times 10^{-8}$, $T_0 = 300$, $b = -0.46$, $E_a = 0.0$	(Semaniak et al., 1998; Sheehan & Maurice, 2004)
C_{23}	$CH_5^+ + e^- \rightarrow CH + 2\,H_2$	$a = 8.7 \times 10^{-9}$, $T_0 = 300$, $b = -0.46$, $E_a = 0.0$	(Semaniak et al., 1998; Sheehan & Maurice, 2004)
C_{24}	$CH_3^+ + e^- \rightarrow CH_2 + H$	$a = 1.28 \times 10^{-7}$, $T_0 = 300$, $b = -0.53$, $E_a = 0.0$	(Sheehan & Maurice, 2004)
C_{25}	$CH_3^+ + e^- \rightarrow CH + H_2$	$a = 4.48 \times 10^{-8}$, $T_0 = 300$, $b = -0.53$, $E_a = 0.0$	(Sheehan & Maurice, 2004)
C_{26}	$CH_3^+ + e^- \rightarrow CH + H$	$a = 5.12 \times 10^{-8}$, $T_0 = 300$, $b = -0.53$, $E_a = 0.0$	(Sheehan & Maurice, 2004)
C_{27}	$CH_3^+ + e^- \rightarrow C + H_2 + H$	$a = 9.6 \times 10^{-8}$, $T_0 = 300$, $b = -0.53$, $E_a = 0.0$	(Sheehan & Maurice, 2004)
C_{28}	$He^+ + e^- \rightarrow He$	$a = 1.77 \times 10^{-10}$, $T_0 = 1$, $b = -0.65$, $E_a = 0.0$	(Millar et al., 1997)
C_{29}	$HeH^+ + e^- \rightarrow He + H$	$a = 3.06 \times 10^{-7}$, $T_0 = 1.0$, $b = -0.6$, $E_a = 0.0$	(Yousif & Mitchell, 1989)
C_{30}	$HeH^+ + C_2H_6 \rightarrow C_2H_5^+ + He + H_2$	$a = 2.1 \times 10^{-9}$, $b = 0.0$, $E_a = 0.0$	(Mackay et al., 1981)
C_{31}	$CH_5^+ + C_2H_4 \rightarrow C_2H_5^+ + CH_4$	$a = 1.5 \times 10^{-9}$, $b = 0.0$, $E_a = 0.0$	(Fiaux et al., 1974)
C_{32}	$CH_5^+ + C_2H_6 \rightarrow C_2H_5^+ + CH_4 + H_2$	$a = 1.215 \times 10^{-9}$, $b = 0.0$, $E_a = 0.0$	(V. G. Anicich, 1993)
C_{33}	$CH_3^+ + CH_4 \rightarrow C_2H_5^+ + H_2$	$a = 1.1 \times 10^{-9}$, $b = 0.0$, $E_a = 0.0$	(V. G. Anicich et al., 2003)
C_{34}	$C_2H_5^+ + e^- \rightarrow C_2H_4 + H$	$a = 7.2 \times 10^{-8}$, $T_0 = 300$, $b = -0.5$, $E_a = 0.0$	(Lehfaoui et al., 1997; Reiter & Janev, 2010)
C_{35}	$C_2H_5^+ + e^- \rightarrow C_2H_3 + H_2$	$a = 3.6 \times 10^{-8}$, $T_0 = 300$, $b = -0.5$, $E_a = 0.0$	(Lehfaoui et al., 1997; Reiter & Janev, 2010)
C_{36}	$C_2H_5^+ + e^- \rightarrow C_2H_3 + 2\,H$	$a = 2.82 \times 10^{-7}$, $T_0 = 300$, $b = -0.5$, $E_a = 0.0$	(Lehfaoui et al., 1997; Reiter & Janev, 2010)
C_{37}	$C_2H_5^+ + e^- \rightarrow C_2H_2 + H_2 + H$	$a = 7.2 \times 10^{-8}$, $T_0 = 300$, $b = -0.5$, $E_a = 0.0$	(Lehfaoui et al., 1997; Reiter & Janev, 2010)
C_{38}	$C_2H_5^+ + e^- \rightarrow C_2H_2 + 3\,H$	$a = 3.6 \times 10^{-8}$, $T_0 = 300$, $b = -0.5$, $E_a = 0.0$	(Lehfaoui et al., 1997; Reiter & Janev, 2010)
C_{39}	$C_2H_5^+ + e^- \rightarrow CH_4 + CH$	$a = 1.2 \times 10^{-8}$, $T_0 = 300$, $b = -0.53$, $E_a = 0.0$	(Lehfaoui et al., 1997; Reiter & Janev, 2010)
C_{40}	$C_2H_5^+ + E \rightarrow CH_3 + CH_2$	$a = 9.0 \times 10^{-8}$, $T_0 = 300$, $b = -0.5$, $E_a = 0.0$	(Lehfaoui et al., 1997; Reiter & Janev, 2010)

Table A5
List of Hydrogen Vibrational Excitation Reactions

Index	Equation	Rate expression
V_1	$H_2 + e_{cr}^- \rightarrow H_2(v) + e_{cr}^-$	(Waite Jr et al., 1983; Egert et al., 2017)
V_2	$2\,H + H_2 \rightarrow H_2(v) + H_2$	(Cravens, 1987)
V_3	$H^+ + H_2(v) \rightarrow H_2^+ + H$	(Huestis et al., 2008; Egert et al., 2017)
V_4	$H_3^+ + e^- \rightarrow H_2(v) + H$	(Cravens, 1987; Florescu-Mitchell & Mitchell, 2006)
V_5	$H_2(v) + H \rightarrow H_2(v\text{-}1) + H$	(Cacciatore et al., 1978; Cravens, 1987)
V_6	$H^+ + H_2(v) \rightarrow H^+ + H_2(v\text{-}1)$	(Egert et al., 2017)
V_7	$H_2 + H_2(v) \leftrightarrow H_2 + H_2(v\text{-}1)$	(Audibert et al., 1973; Shull & Hollenbach, 1978)
V_8	$H_2(v) + H_2(w) \leftrightarrow H_2(v\text{-}1) + H_2(w{+}1)$	(Billing & Fisher, 1976; Gordiets et al., 1974)

Appendix B: UV Emission and Color Ratio

The partitioning of total energy deposition into UV Lyman and Werner band emission rates provides an estimate of the UV emission spectrum and corresponding Color Ratio. We adopted laboratory measurements of the H_2 UV emission spectrum ($U(\nu)$) between 120–160 nm (Liu et al., 1995). The relative intensities of emission spectrum are normalized and the normalized intensities are used for generating UV emission spectra at each height grid through the atmospheric column. We simulate the UV radiative transfer throughout the atmospheric column to

project top of atmosphere (TOA) UV emission in kR units. Volumetric production rate (J_{prod}) at each point is geometric mean of the surrounding top and bottom grid points. It is integrated over each grid point integrated over the atmospheric column to provide TOA UV emission (I_ν).

$$I_\nu = \int_{base}^{TOA} J_{prod}(z,\nu) e^{-\tau(z,\nu)} dz \tag{B1}$$

$$J_{prod}(z,\nu) = U(\nu)\phi_{UV}E(z) \tag{B2}$$

Here, $\tau(z,\nu)$ is the total monochromatic opacity from eac grid point to TOA. It is represented as sum of H_2, He, CH_4 and C_2H_2 opacities, each consisting of UV absorption cross section adopted from the Leiden photochemical database. For H_2 and He, we add the Rayleigh scattering cross-section to the opacity. ϕ_{UV} is percent of total energy (E) that goes into Lyman and Wener band emissions. It is assumed to be 18% based on the two-stream electron transport (Waite et al., 1983).

The PJ 7 event amounts to an emission of few thousands kR at the long wavelengths between 150–160 nm (Figure B1). The corresponding UV color ratio amounts to a value of 20, consistent with the high color ratio observations by Juno UVS at the northern aurora (G. Gladstone et al., 2017; Benmahi et al., 2024). It is to be noted that the color ratio calculations represent contribution from JEDI and UVS derived electron flux. Addition of JADE electron flux can elevate the UV emission. At pressure levels deeper than 0.01 mbar, the atmospheric column absorbs all UV emissions below 150 nm. Near-complete absorption of UV emission below 150 nm influences the relative intensity of TOA emission.

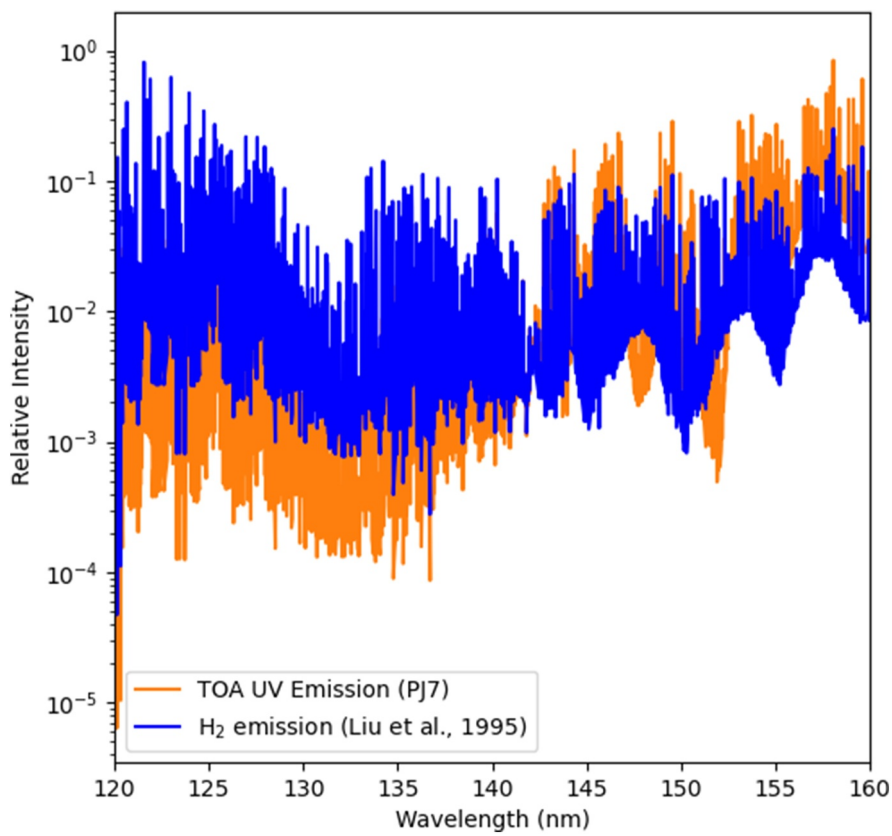


Figure B1. Relative intensity of TOA UV emission due to precipitation of high-energy electrons with energies up to 10 MeV. We apply the PJ 7 JEDI and UVS derived downward electron energy flux to estimate H_2 UV emission. The TOA emission intensity values are compared with input laboratory based H_2 emission intensities (Liu et al., 1995).

Data Availability Statement

The calibrated data for the Juno MicroWave Radiometer instrument during the orbits PJ 1, 3 to 54 is publicly available on the NASA Planetary Data System. Chemical kinetics code (C^3M) for simulating ionospheric chemistry (Bhattacharya & Li, 2024) can be accessed through the following GitHub repository: https://github.com/GalacticBobster/C3M/tree/ion. It also stores corresponding metadata, input files for reaction network, and relevant rate coefficients. C^3M outputs are stored in netCDF format, and they can be accessed on Zenodo (Bhattacharya, 2025). The python code for CSDA, and plotting the NetCDF output files are available on GitHub: https://github.com/GalacticBobster/Jupiter-Auroral-Energy-Deposition. Microwave opacity model for estimating the microwave attenuation and brightness temperature has been made publicly available at https://github.com/ylu484/Jupiter-MWR-Attenuation-Yue.

Acknowledgments
This work was supported by the NASA Juno Program, under NASA Contract NNM06AA75C from the Marshall Space Flight Center supporting the Juno Mission Science team, through subcontract 699056KC and Q99063JAR to the University of Michigan from the Southwest Research Institute. A portion of this research was carried out at the Jet Propulsion Laboratory, California Institute of Technology, under a contract with the National Aeronautics and Space Administration (80NM0018D0004).

References

Achilleos, N., Miller, S., Prangé, R., Millward, G., & Dougherty, M. (2001). A dynamical model of jupiter's auroral electrojet. *New Journal of Physics*, *3*(1), 303. https://doi.org/10.1088/1367-2630/3/1/303

Agostinelli, S., Allison, J., Amako, K. a., Apostolakis, J., Araujo, H., Arce, P., et al. (2003). Geant4—A simulation toolkit. *Nuclear Instruments and Methods in Physics Research Section A: Accelerators, Spectrometers, Detectors and Associated Equipment*, *506*(3), 250–303. https://doi.org/10.1016/s0168-9002(03)01368-8

Allen, M., Yung, Y. L., & Gladstone, G. R. (1992). The relative abundance of ethane to acetylene in the jovian stratosphere. *Icarus*, *100*(2), 527–533. https://doi.org/10.1016/0019-1035(92)90115-n

Anicich, V., Huntress, W., et al. (1979). An ion cyclotron resonance study of reactions of ions with hydrogen atomsa. *The Journal of Chemical Physics*, *70*(6), 2877–2881. https://doi.org/10.1063/1.437823

Anicich, V. G. (1993). Evaluated bimolecular ion-molecule gas phase kinetics of positive ions for use in modeling planetary atmospheres, cometary comae, and interstellar clouds. *Journal of Physical and Chemical Reference Data*, *22*(6), 1469–1569. https://doi.org/10.1063/1.555940

Anicich, V. G., Wilson, P., & McEwan, M. J. (2003). Termolecular ion-molecule reactions in titan's atmosphere. iv. a search made at up to 1 micron in pure hydrocarbons. *Journal of the American Society for Mass Spectrometry*, *14*(8), 900–915. https://doi.org/10.1016/s1044-0305(03)00218-6

Aquilanti, V., Galli, A., Giardini-Guidoni, A., & Volpi, G. G. (1965). Ion—Molecule reactions in hydrogen—Rare-gas mixtures. *The Journal of Chemical Physics*, *43*(6), 1969–1973. https://doi.org/10.1063/1.1697061

Atreya, S., & Donahue, T. (1975). Ionospheric models of saturn, uranus, and neptune. *Icarus*, *24*(3), 358–362. https://doi.org/10.1016/0019-1035(75)90131-1

Atreya, S. K., & Donahue, T. M. (1975). The role of hydrocarbons in the ionospheres of the outer planets. *Icarus*, *25*(2), 335–338. https://doi.org/10.1016/0019-1035(75)90027-5

Audibert, M.-M., Joffrin, C., & Ducuing, J. (1973). Vibrational relaxation in hydrogen-rare-gases mixtures. *Chemical Physics Letters*, *19*(1), 26–28. https://doi.org/10.1016/0009-2614(73)87053-8

Banks, P. (1966). Collision frequencies and energy transfer electrons. *Planetary and Space Science*, *14*(11), 1085–1103. https://doi.org/10.1016/0032-0633(66)90024-9

Baulch, D., Cobos, C., Cox, R., Esser, C., Frank, P., & Just, T. (1992). Evaluated kinetic data for combustion modelling.

Baulch, D., Cobos, J., Cox, A., Frank, P., Hayman, G., Just, T., et al. (1994). Summary table of evaluated kinetic data for combustion modelling: Supplement 1. *Combustion and Flame*, *98*(1–2), 59–79. https://doi.org/10.1016/0010-2180(94)90198-8

Becker, K., Engelhardt, B., Wiesen, P., & Bayes, K. (1989). Rate constants for ch (x 2\pi) reactions at low total pressures. *Chemical Physics Letters*, *154*(4), 342–348. https://doi.org/10.1016/0009-2614(89)85367-9

Benmahi, B., Bonfond, B., Benne, B., Grodent, D., Hue, V., Gladstone, G., et al. (2024). Energy mapping of jupiter's auroral electrons from juno/uvs data using a new h2 uv emission model. *Astronomy and Astrophysics*, *685*, A26. https://doi.org/10.1051/0004-6361/202348634

Berman, M. R., Fleming, J., Harvey, A., & Lin, M.-C. (1982). Temterature dependence of the reactions of ch radicals with unsaturated hydrocarbons. *Chemical Physics*, *73*(1–2), 27–33. https://doi.org/10.1016/0301-0104(82)85147-1

Bhattacharya, A. (2025). Jupiter's auroral ionosphere: High-energy electron precipitation event output. *Zenodo*. https://doi.org/10.5281/zenodo.14774920

Bhattacharya, A., & Li, C. (2024). Galacticbobster/c3m: V1.0.0-jup. *Zenodo*. https://doi.org/10.5281/zenodo.13625145

Billing, G. D., & Fisher, E. R. (1976). Vv and vt rate coefficients in h2 by a quantum-classical model. *Chemical Physics*, *18*(1–2), 225–232. https://doi.org/10.1016/0301-0104(76)87049-8

Böhland, T., Temps, F., & Wagner, H. G. (1985). The contributions of intersystem crossing and reaction in the removal of ch2 (ã1a1) by hydrocarbons studied with the lmr. *Berichte der Bunsen-Gesellschaft für Physikalische Chemie*, *89*(9), 1013–1018. https://doi.org/10.1002/bbpc.19850890917

Bonfond, B., Gladstone, G., Grodent, D., Gérard, J.-C., Greathouse, T., Hue, V., et al. (2018). Bar code events in the juno-uvs data: Signature 10 mev electron microbursts at jupiter. *Geophysical Research Letters*, *45*(22), 12–108. https://doi.org/10.1029/2018gl080490

Bonfond, B., Saur, J., Grodent, D., Badman, S., Bisikalo, D., Shematovich, V., et al. (2017). The tails of the satellite auroral footprints at jupiter. *Journal of Geophysical Research: Space Physics*, *122*(8), 7985–7996. https://doi.org/10.1002/2017ja024370

Brownsword, R. A., Canosa, A., Rowe, B. R., Sims, I. R., Smith, I. W., Stewart, D. W., et al. (1997). Kinetics over a wide range of temperature (13–744 k): Rate constants for the reactions of ch (\nu= 0) with h2 and d2 and for the removal of ch (\nu= 1) by h2 and d2. *Journal of Chemical Physics*, *106*(18), 7662–7677. https://doi.org/10.1063/1.473750

Cacciatore, M., Capitelli, M., & Dilonardo, M. (1978). A joint vibro-electronic mechanism in the dissociation of molecular hydrogen in nonequilibrium plasmas. *Chemical Physics*, *34*(2), 193–204. https://doi.org/10.1016/0301-0104(78)80035-4

Canosa, A., Sims, I. R., Travers, D., Smith, I. W., & Rowe, B. (1997). Reactions of the methylidine radical with ch_4_, c_2_h_2_, c_2_h_4_, c_2_h_6_, and but-1-ene studied between 23 and 295k with a cresu apparatus. *Astronomy and Astrophysics*, *323*, 644–651.

Clark, G., Tao, C., Mauk, B., Nichols, J., Saur, J., Bunce, E., et al. (2018). Precipitating electron energy flux and characteristic energies in jupiter's main auroral region as measured by juno/jedi. *Journal of Geophysical Research: Space Physics*, *123*(9), 7554–7567. https://doi.org/10.1029/2018ja025639

Cravens, T. (1987). Vibrationally excited molecular hydrogen in the upper atmosphere of jupiter. *Journal of Geophysical Research*, *92*(A10), 11083–11100. https://doi.org/10.1029/ja092ia10p11083

Desorgher, L., Flückiger, E. O., Gurtner, M., Moser, M. R., & Bütikofer, R. (2005). Atmocosmics: A geant 4 code for computing the interaction of cosmic rays with the earth's atmosphere. *International Journal of Modern Physics A*, *20*(29), 6802–6804. https://doi.org/10.1142/S0217751X05030132

Drossart, P., Bézard, B., Atreya, S. K., Bishop, J., Waite Jr, J., & Boice, D. (1993). Thermal profiles in the auroral regions of jupiter. *Journal of Geophysical Research*, *98*(E10), 18803–18811. https://doi.org/10.1029/93je01801

Ebert, R., Greathouse, T., Clark, G., Allegrini, F., Bagenal, F., Bolton, S., et al. (2019). Comparing electron energetics and uv brightness in jupiter's northern polar region during juno perijove 5. *Geophysical Research Letters*, *46*(1), 19–27. https://doi.org/10.1029/2018gl081129

Egert, A., Waite Jr, J. H., & Bell, J. (2017). Applications of the jupiter global ionosphere-thermosphere model: A case study of auroral electron energy deposition. *Journal of Geophysical Research: Space Physics*, *122*(2), 2210–2236. https://doi.org/10.1002/2016ja023189

Fahr, A., Laufer, A., Klein, R., & Braun, W. (1991). Reaction rate determinations of vinyl radical reactions with vinyl, methyl, and hydrogen atoms. *Journal of Physical Chemistry*, *95*(8), 3218–3224. https://doi.org/10.1021/j100161a047

Fahr, A., & Laufer, A. H. (1995). Deuterium isotope effect in vinyl radical combination/disproportionation reactions. *Journal of Physical Chemistry*, *99*(1), 262–264. https://doi.org/10.1021/j100001a040

Fiaux, A., Smith, D., & Futrell, J. (1974). Reaction of ch5+ with c2h2, c2h4, c3h6 and c-c3h6. *International Journal of Mass Spectrometry and Ion Physics*, *15*(1), 9–21. https://doi.org/10.1016/0020-7381(74)80082-3

Florescu-Mitchell, A., & Mitchell, J. B. A. (2006). Dissociative recombination. *Physics Reports*, *430*(5–6), 277–374. https://doi.org/10.1016/j.physrep.2006.04.002

Gérard, J.-C., Gkouvelis, L., Bonfond, B., Gladstone, G., Mura, A., Adriani, A., et al. (2023). H3+ cooling in the jovian aurora: Juno remote sensing observations and modeling. *Icarus*, *389*, 115261. https://doi.org/10.1016/j.icarus.2022.115261

Gladstone, G., Versteeg, M., Greathouse, T., Hue, V., Davis, M., Gérard, J.-C., et al. (2017). Juno-uvs approach observations of jupiter's auroras. *Geophysical Research Letters*, *44*(15), 7668–7675. https://doi.org/10.1002/2017gl073377

Gladstone, G. R., Allen, M., & Yung, Y. (1996). Hydrocarbon photochemistry in the upper atmosphere of jupiter. *Icarus*, *119*(1), 1–52. https://doi.org/10.1006/icar.1996.0001

Glosik, J., Plasil, R., Pysanenko, A., Novotnỳ, O., Hlavenka, P., Macko, P., & Bánó, G. (2005). Recombination studies in a he-ar-h2 plasma. *Journal of Physics: Conference Series*, *4*, 104–110. https://doi.org/10.1088/1742-6596/4/1/014

Goodwin, D. G., Moffat, H. K., Schoegl, I., Speth, R. L., & Weber, B. W. (2024). Cantera: An object-oriented software toolkit for chemical kinetics, thermodynamics, and transport processes. https://doi.org/10.5281/zenodo.8137090

Gordiets, B., Mamedov, S. S., & Shelepin, L. (1974). Vibrational kinetics of anharmonic oscillators under essentially nonequilibrium conditions. *Zhurnal Eksperimental'noi i Teoreticheskoi Fiziki*, *67*, 1287–1300.

Harada, Y., Nakamura, Y., Sánchez-Cano, B., Lester, M., Terada, N., & Leblanc, F. (2023). Radio absorption in the nightside ionosphere of mars during solar energetic particle events. *Space Weather*, *21*(12), e2023SW003755. https://doi.org/10.1029/2023sw003755

Hargreaves, J. (1969). Auroral absorption of hf radio waves in the ionosphere: A review of results from the first decade of riometry. *Proceedings of the IEEE*, *57*(8), 1348–1373. https://doi.org/10.1109/proc.1969.7275

Hodges, A., Steffes, P., Bellotti, A., Waite, J. H., Brown, S., Oyafuso, F., et al. (2020). Observations and electron density retrievals of jupiter's discrete auroral arcs using the juno microwave radiometer. *Journal of Geophysical Research: Planets*, *125*(9), e2019JE006293. https://doi.org/10.1029/2019je006293

Hu, R., Seager, S., & Bains, W. (2012). Photochemistry in terrestrial exoplanet atmospheres. i. photochemistry model and benchmark cases. *The Astrophysical Journal*, *761*(2), 166. https://doi.org/10.1088/0004-637x/761/2/166

Huestis, D. L., Bougher, S. W., Fox, J. L., Galand, M., Johnson, R. E., Moses, J. I., & Pickering, J. C. (2008). Cross sections and reaction rates for comparative planetary aeronomy. *Comparative Aeronomy*, *139*(1–4), 63–105. https://doi.org/10.1007/s11214-008-9383-7

Janssen, M., Oswald, J., Brown, S., Gulkis, S., Levin, S., Bolton, S., et al. (2017). Mwr: Microwave radiometer for the juno mission to jupiter. *Space Science Reviews*, *213*(1–4), 139–185. https://doi.org/10.1007/s11214-017-0349-5

Kim, J., & Huntress, W. (1975). Ion cyclotron resonance studies on the reaction of h2+ and d2+ ions with various simple molecules and hydrocarbons. *The Journal of Chemical Physics*, *62*(7), 2820–2825. https://doi.org/10.1063/1.430817

Kim, Y., & Fox, J. L. (1994). The chemistry of hydrocarbon ions in the jovian ionosphere. *Icarus*, *112*(2), 310–325. https://doi.org/10.1006/icar.1994.1186

Krasnopolsky, V. A. (2019). *Spectroscopy and photochemistry of planetary atmospheres and ionospheres: Mars, venus, titan, triton and pluto* (Vol. 23). Cambridge University Press. https://doi.org/10.1017/9781316535561

Lehfaoui, L., Rebrion-Rowe, C., Laubé, S., Mitchell, J., & Rowe, B. (1997). The dissociative recombination of hydrocarbon ions. i. light alkanes. *Journal of Chemical Physics*, *106*(13), 5406–5412. https://doi.org/10.1063/1.473566

Li, C., & Chen, X. (2019). Simulating nonhydrostatic atmospheres on planets (snap): Formulation, validation, and application to the jovian atmosphere. *The Astrophysical Journal - Supplement Series*, *240*(2), 37. https://doi.org/10.3847/1538-4365/aafdaa

Li, C., Ingersoll, A., Janssen, M., Levin, S., Bolton, S., Adumitroaie, V., et al. (2017). The distribution of ammonia on jupiter from a preliminary inversion of juno microwave radiometer data. *Geophysical Research Letters*, *44*(11), 5317–5325. https://doi.org/10.1002/2017gl073159

Liu, X., Ahmed, S. M., Multari, R. A., James, G. K., & Ajello, J. M. (1995). High-resolution electron-impact study of the far-ultraviolet emission spectrum of molecular hydrogen. *Astrophysical Journal Supplement*, *v. 101*, 101–375. https://doi.org/10.1086/192246

Mackay, G., Schiff, H., & Bohme, D. (1981). A room-temperature study of the kinetics and energetics for the protonation of ethane. *Canadian Journal of Chemistry*, *59*(12), 1771–1778. https://doi.org/10.1139/v81-265

Mannucci, A., Tsurutani, B., Verkhoglyadova, O., Komjathy, A., & Pi, X. (2015). Use of radio occultation to probe the high latitude ionosphere. *Atmospheric Measurement Techniques Discussions*, *8*(2), 2093–2121. https://doi.org/10.5194/amt-8-2789-2015

Mauk, B., Haggerty, D., Paranicas, C., Clark, G., Kollmann, P., Rymer, A., et al. (2017a). Juno observations of energetic charged particles over jupiter's polar regions: Analysis of monodirectional and bidirectional electron beams. *Geophysical Research Letters*, *44*(10), 4410–4418. https://doi.org/10.1002/2016gl072286

Mauk, B., Haggerty, D., Paranicas, C., Clark, G., Kollmann, P., Rymer, A., et al. (2018). Diverse electron and ion acceleration characteristics observed over jupiter's main aurora. *Geophysical Research Letters*, *45*(3), 1277–1285. https://doi.org/10.1002/2017gl076901

Mauk, B., Szalay, J., Allegrini, F., Bagenal, F., Bolton, S., Clark, G., et al. (2023). How bi-modal are jupiter's main aurora zones? *Journal of Geophysical Research: Space Physics*, *128*(4), e2022JA031237. https://doi.org/10.1029/2022ja031237

Mauk, B. H., Clark, G., Gladstone, G. R., Kotsiaros, S., Adriani, A., Allegrini, F., et al. (2020). Energetic particles and acceleration regions over jupiter's polar cap and main aurora: A broad overview. *Journal of Geophysical Research: Space Physics*, *125*(3), e2019JA027699. https://doi.org/10.1029/2019ja027699

Mauk, B. H., Haggerty, D., Paranicas, C., Clark, G., Kollmann, P., Rymer, A., et al. (2017b). Discrete and broadband electron acceleration in jupiter's powerful aurora. *Nature*, *549*(7670), 66–69. https://doi.org/10.1038/nature23648

McCall, B., Huneycutt, A., Saykally, R., Djuric, N., Dunn, G., Semaniak, J., et al. (2004). Dissociative recombination of rotationally cold h 3+. Physical review A—Atomic. *Molecular, and Optical Physics*, *70*(5), 052716. https://doi.org/10.1103/physreva.70.052716

Mendillo, M., Narvaez, C., Moore, L., & Withers, P. (2022). Jupiter's enigmatic ionosphere: Electron density profiles from the pioneer, voyager, and galileo radio occultation experiments. *Journal of Geophysical Research: Planets*, *127*(3), e2021JE007169. https://doi.org/10.1029/2021je007169

Millar, T., Farquhar, P., & Willacy, K. (1997). The umist database for astrochemistry 1995. *Astronomy & Astrophysics Supplement Series*, *121*(1), 139–185. https://doi.org/10.1051/aas:1997118

Miller, T. M., Moseley, J., Martin, D., & McDaniel, E. (1968). Reactions of h+ in h 2 and d+ in d 2; mobilities of hydrogen and alkali ions in h 2 and d 2 gases. *Physical Review*, *173*(1), 115.

Mitchell, J. (1990). The dissociation recombination of molecules. *Physics Reports*, *186*, 216–248.

Moses, J. I., Bézard, B., Lellouch, E., Gladstone, G. R., Feuchtgruber, H., & Allen, M. (2000). Photochemistry of saturn's atmosphere: I. Hydrocarbon chemistry and comparisons with iso observations. *Icarus*, *143*(2), 244–298. https://doi.org/10.1006/icar.1999.6270

Moses, J. I., Fouchet, T., Yelle, R. V., Friedson, A. J., Orton, G. S., Bézard, B., et al. (2004). The stratosphere of jupiter. *Jupiter: Planet, Satellites and Magnetosphere*, 129–157.

Moses, J. I., & Poppe, A. R. (2017). Dust ablation on the giant planets: Consequences for stratospheric photochemistry. *Icarus*, *297*, 33–58. https://doi.org/10.1016/j.icarus.2017.06.002

Nakamura, Y., Terada, K., Tao, C., Terada, N., Kasaba, Y., Leblanc, F., et al. (2022). Effect of meteoric ions on ionospheric conductance at jupiter. *Journal of Geophysical Research: Space Physics*, *127*(3), e2022JA030312. https://doi.org/10.1029/2022ja030312

Nordheim, T., Dartnell, L., Desorgher, L., Coates, A. J., & Jones, G. H. (2015). Ionization of the venusian atmosphere from solar and galactic cosmic rays. *Icarus*, *245*, 80–86. https://doi.org/10.1016/j.icarus.2014.09.032

Oyafuso, F., Levin, S., Orton, G., Brown, S. T., Adumitroaie, V., Janssen, M., et al. (2020). Angular dependence and spatial distribution of jupiter's centimeter-wave thermal emission from juno's microwave radiometer. *Earth and Space Science*, *7*(11), e2020EA001254. https://doi.org/10.1029/2020ea001254

Oyafuso, F. A., Levin, S., Waite, J. H., Steffes, P., & Bolton, S. (2023). Analysis of the effect of jupiter's northern aurora on juno microwave radiometer observations. In *Egu general assembly conference abstracts*. EGU–10437).

Padovani, M., Galli, D., & Glassgold, A. E. (2009). Cosmic-ray ionization of molecular clouds. *Astronomy and Astrophysics*, *501*(2), 619–631. https://doi.org/10.1051/0004-6361/200911794

Perry, J., Kim, Y., Fox, J. L., & Porter, H. (1999). Chemistry of the jovian auroral ionosphere. *Journal of Geophysical Research*, *104*(E7), 16541–16565. https://doi.org/10.1029/1999je900022

Pinto, C., & Galli, D. (2008). Three-fluid plasmas in star formation-ii. momentum transfer rate coefficients. *Astronomy and Astrophysics*, *484*(1), 17–28. https://doi.org/10.1051/0004-6361:20078819e

Praxmarer, C., Hansel, A., & Lindinger, W. (1994). Interaction between the ion dipole and the ion-induced dipole in reactions of the polar ion arh+ 3. *Journal of Chemical Physics*, *100*(12), 8884–8889. https://doi.org/10.1063/1.466691

Reiter, D., & Janev, R. (2010). Hydrocarbon collision cross sections for magnetic fusion: The methane, ethane and propane families. *Contributions to Plasma Physics*, *50*(10), 986–1013. https://doi.org/10.1002/ctpp.201000090

Rogers, A. E., Bowman, J. D., Vierinen, J., Monsalve, R., & Mozdzen, T. (2015). Radiometric measurements of electron temperature and opacity of ionospheric perturbations. *Radio Science*, *50*(2), 130–137. https://doi.org/10.1002/2014rs005599

Romani, P. N. (1996). Recent rate constant and product measurements of the reactions c2h3+ h2and c2h3+ h—Importance for photochemical modeling of hydrocarbons on jupiter. *Icarus*, *122*(2), 233–241. https://doi.org/10.1006/icar.1996.0122

Romani, P. N., Bishop, J., Bézard, B., & Atreya, S. (1993). Methane photochemistry on neptune: Ethane and acetylene mixing ratios and haze production. *Icarus*, *106*(2), 442–463. https://doi.org/10.1006/icar.1993.1184

Salveter, A., Saur, J., Clark, G., & Mauk, B. (2022). Jovian auroral electron precipitation budget—A statistical analysis of diffuse, monoenergetic, and broadband auroral electron distributions. *Journal of Geophysical Research: Space Physics*, *127*(8), e2021JA030224. https://doi.org/10.1029/2021ja030224

Semaniak, J., Larson, A., Le Padellec, A., Stromholm, C., Larsson, M., Rosen, S., et al. (1998). Dissociative recombination and excitation of ch5+: Absolute cross sections and branching fractions. *The Astrophysical Journal*, *498*(2), 886–895. https://doi.org/10.1086/305581

Sheehan, C., & Maurice, J.-P. S. (2004). Dissociative recombination of the methane family ions: Rate coefficients and implications. *Advances in Space Research*, *33*(2), 216–220. https://doi.org/10.1016/j.asr.2003.07.019

Shull, J. M., & Hollenbach, D. J. (1978). H2 cooling, dissociation, and infrared emission in shocked molecular clouds. *The Astrophysical Journal*, *220*(Mar. 1), 525–537. https://doi.org/10.1086/155934

Sinclair, J., Orton, G., Greathouse, T., Fletcher, L., Moses, J., Hue, V., & Irwin, P. (2017). Jupiter's auroral-related stratospheric heating and chemistry i: Analysis of voyager-iris and cassini-cirs spectra. *Icarus*, *292*, 182–207. https://doi.org/10.1016/j.icarus.2016.12.033

Song, M.-Y., Yoon, J.-S., Cho, H., Itikawa, Y., Karwasz, G. P., Kokoouline, V., et al. (2015). Cross sections for electron collisions with methane. *Journal of Physical and Chemical Reference Data*, *44*(2), 6–8. https://doi.org/10.1063/1.4918630

Waite, J., Cravens, T., Kozyra, J., Nagy, A., Atreya, S., & Chen, R. (1983). Electron precipitation and related aeronomy of the jovian thermosphere and ionosphere. *Journal of Geophysical Research*, *88*(A8), 6143–6163. https://doi.org/10.1029/ja088ia08p06143

Wang, B., Hou, H., Yoder, L. M., Muckerman, J. T., & Fockenberg, C. (2003). Experimental and theoretical investigations on the methyl-methyl recombination reaction. *The Journal of Physical Chemistry A*, *107*(51), 11414–11426. https://doi.org/10.1021/jp030657h

Woo, W., & DeGroot, J. (1984). Microwave absorption and plasma heating due to microwave breakdown in the atmosphere. *The Physics of Fluids*, *27*(2), 475–487. https://doi.org/10.1063/1.864645

Yousif, F., & Mitchell, J. (1989). Recombination and excitation of heh+. *Physical Review A*, *40*(8), 4318–4321. https://doi.org/10.1103/physreva.40.4318

Yung, Y. L., Allen, M., & Pinto, J. P. (1984). Photochemistry of the atmosphere of titan-comparison between model and observations. *The Astrophysical Journal - Supplement Series*, *55*(55), 465–506. (ISSN 0067-0049). https://doi.org/10.1086/190963

Zhu, B., Lindstrom, C., Jun, I., Garrett, H., Kollmann, P., Paranicas, C., et al. (2021). Jupiter high-energy/high-latitude electron environment from juno's jedi and uvs science instrument background noise. *Nuclear Instruments and Methods in Physics Research Section A: Accelerators, Spectrometers, Detectors and Associated Equipment*, *1002*, 165244. https://doi.org/10.1016/j.nima.2021.165244